FEMTOSECOND TIME-RESOLVED SPECTROSCOPY OF COHERENT OSCILLATIONS IN NANOMATERIALS

A Dissertation

by

SERGUEI JEREBTSOV

Submitted to the Office of Graduate Studies of
Texas A&M University
in partial fulfillment of the requirements for the degree of

DOCTOR OF PHILOSOPHY

May 2007

Major Subject: Physics

FEMTOSECOND TIME-RESOLVED SPECTROSCOPY OF COHERENT OSCILLATIONS IN NANOMATERIALS

A Dissertation

by

SERGUEI JEREBTSOV

Submitted to the Office of Graduate Studies of
Texas A&M University
in partial fulfillment of the requirements for the degree of

DOCTOR OF PHILOSOPHY

Approved by:

Chair of Committee,	Hans A. Schuessler
Committee Members,	Glenn Agnolet
	Gerhard Paulus
	Raymond Schaak
Head of Department,	Edward Fry

May 2007

Major Subject: Physics

ABSTRACT

Femtosecond Time-resolved Spectroscopy of Coherent Oscillations in Nanomaterials.

(May 2007)

Serguei Jerebtsov, B.S., Moscow Institute of Engineering and Physics

Chair of Advisory Committee: Dr. Hans A. Schuessler

The interaction of laser radiation with a material can excite coherent lattice vibration. The observation of such periodic motion of the atoms in the lattice provides information on the properties of the material. In the present work a femtosecond pump-probe technique was applied for studies of acoustic vibrations in nanoparticles and nanowires, and coherent optical phonons in thin films.

The elastic properties of spherical Ag nanoparticles and Ag and Bi nanowires were studied in a dual-color femtosecond pump-probe experiment. The results of the period determinations of the acoustic vibrations, obtained from the time-domain measurements with low intensity pump pulses, together with the information about the size of the particles, were used to determine the elastic constants of the materials. Also changes in the measured acoustical response of the Ag nanowires under high intensity laser excitation were studied.

In addition the coherent optical phonon excitation in a Bi film was studied in a femtosecond pump-probe experiment. A red-shift of the phonon frequency at the high photoexcitation density was observed. To separate the effect of the lattice softening and the lattice anharmonicity the excitation with two pump pulses was employed. Numerical simulations, which took into account the evolution of the spatial inhomogeneity of the excitation density, were carried out and compared to the experimental results.

ACKNOWLEDGMENTS

First of all, I would like to thank my advisor Dr. Hans A. Schuessler who initiated this research. Without him, this work would not be possible. I am greatly indebted to Dr. Alexander Kolomenskii for all his help during my years here.

I would also like to express my appreciation to all of the wonderful people who have worked in this lab over the years: Vladimir Ryjkov, Xianzhen Zhao, Vladimir Lioubimov, Feng Zhu, Andreas Mershin, and Milan Poudel. It has been a pleasure to share the lab with you.

The Department of Physics, Texas A&M University also has my thanks for the financial support during these years. I would like to thank our staff, especially Sandi Smith, for their continuous assistance to students with administrative matters.

TABLE OF CONTENTS

CHAPTER Page

LIST OF TABLES

LIST OF FIGURES

FIGURE Page

FIGURE Page

FIGURE Page

CHAPTER I

INTRODUCTION

The interaction of laser radiation with matter produces coherent lattice vibrations. These vibrations can be in the form of coherent bulk and surface acoustic waves which were extensively used for the determination of elastic properties of bulk materials. The laser generated surface acoustic waves can be employed for contact free diagnostics of materials, when the detection is also performed optically by a probe laser beam. The confinement of this wave in a small sub-surface layer concentrates the acoustic energy and makes it possible to reach the nonlinear regime of the wave propagation [1, 2, 3].

In my initial research, I investigated linear and nonlinear properties of laser-generated surface acoustic waves. The interaction of nanosecond and femtosecond laser pulses with metals and semiconductors were studied and the results of this earlier work are presented in Appendices B, C, and D.

Recently, different methods of production of nanomaterials, including nanoparticles and nanowires were developed [4, 5, 6]. Many phenomena studied for bulk materials also take place at the nanoscale, but they are affected by the size and shape of the nanoparticles[7, 8, 9, 10]. The acoustic response of nano-objects exhibits discrete frequency modes due to the confinement of acoustic vibrations at relatively high frequencies on the order of 100 MHz [11, 12, 13].

In the initial stage of the interaction process, non-equilibrium phenomena take place such as the thermalization of the electronic sub-system and the energy transfer to the lattice via electron-phonon coupling. This fast dynamics occurs on the

---

The journal model is Physical Review Letters.

femtosecond time scale. In the materials with more than one atom in the primitive cell, the optical phonons, which correspond to the vibrations of the adjacent atoms in opposite directions with typical frequencies of a few THz, can also be excited. For studying these fast dynamic processes a femtosecond pump-probe technique was used in my research. In this approach a strong laser pulse (pump) excites the lattice vibrations and a delayed laser pulse (probe) detects them after some time has elapsed. In this way information on the elastic and thermodynamic properties of the material can be obtained. For this work a femtosecond oscillator with the Kerr-lens mode-locking was employed. The investigation of transitional states of matter and relaxation processes at high levels of electronic excitations was done by amplifying the pulses from the oscillator in a regenerative amplifier. This also allowed the observation of nonlinear effects related to the transient softening of the lattice. The principles of the related femtosecond laser technology are described in Chapter II.

The measured response of nanomaterials provides information on their elastic properties provided that the size and the shape of the nano-objects is known or determined independently, i.e. by electron microscopy. In the simplest case of a spherical particle the oscillation frequencies are described by the formulas derived by Lamb [14]. This formula was generalized to the case when the surrounding medium is taken into account[15, 16]. Also the description for more complex configurations, such as nanorods, was obtained. Nanowires, studied in this work, can be considered as the limiting case of a rod with a high aspect ratio. In the laser pump-probe experiments, the highly symmetric (breathing) mode is observed. Unlike previous experiments, the measurements were performed not only in transmission but also with scattered light. The theoretical description and experimental investigations of Ag nanoparticles and Ag and Bi nanowires, including fast non-equilibrium dynamics and acoustic modes are presented in Chapter III.

For the excitation of optical phonons, the excitation pulse should be short enough and contain substantial spectral components at the optical phonon frequency. The excitation takes place due to a displacive mechanism (in strongly absorbing materials) or impulsive mechanism (in transparent materials). As was recently shown, both situations can be considered as particular cases of the Impulsive Stimulated Raman Scattering (ISRS) mechanism [17]. This more general approach explains why, in addition to the symmetric breathing A1 mode, the Eg mode with the non-diagonal components of the Raman tensor can be observed in the pump-probe experiments. Coherent optical phonons were studied in Bi. In this semimetal, a short femtosecond pump pulse promotes electrons from the valence band to the conduction band. That causes a shift in the equilibrium positions of the atoms in the lattice and thereby generating coherent lattice vibrations. These oscillations induce a change in the refractive index of the material and can be seen as a modulation in the reflected or scattered light. At the high level of the excitation the reduction of the phonon mode frequency was observed. Two effects can affect the observed oscillation frequency: the excitation density and the acoustic nonlinearity. To separate these effects, the excitation with two pump pulses was carried out. We performed modeling of the signals observed in the pump-probe experiments at high excitation levels taking into account the excitation inhomogeneity. By comparing with the experimental results we concluded that the major contribution to the decay of the observed oscillations is due to the strong inhomogeneity and that the dynamics of the frequency shift can be solely explained by the lattice softening and its evolution. The studies of the optical phonons are considered in Chapter IV.

In the end of the dissertation a Conclusion is presented followed by the Appendix A (the scanning electron and transmission electron micrographs of the studied nanomaterials) and the Appendices B,C, and D (studies of the laser-excited surface

acoustic waves in bulk materials).

CHAPTER II

FEMTOSECOND LASER TECHNIQUE IN A PUMP-PROBE EXPERIMENT

For studies of the coherent lattice vibrations in nanomaterials the femtosecond pump-probe technique was employed. This method has high temporal resolution which is limited by the duration of the laser pulse. Also the high peak intensity of the laser pulses make it possible to excite the material to a highly nonequilibrium state.

This chapter has the following structure: the basic aspects of the femtosecond laser pulse generation and the laser pulse characterization are discussed first, followed by the description of the femtosecond laser system used in the experiments. The transient transmission setup is described in the third part. In the experiments with nanowires and Bi films the detection arrangement of the experimental setup was adapted to the changed requirements. These modifications are described in the corresponding experimental sections of Chapter III and Chapter IV.

A. Femtosecond Laser Pulse Generation

1. The time-bandwidth product

The electric field of a laser pulse can be written as [18]

$$E(t) = \frac{1}{2}\mathcal{E}(t)e^{i(\omega_l t+\varphi(t))} + c.c., \tag{2.1}$$

where $\mathcal{E}(t)$ is the field envelope, ω_l is the carrier frequency, and $\varphi(t)$ is the time dependent phase (Fig. 1). The first derivative of the phase factor in the above formula defines the time dependent carrier frequency $\omega(t) = \omega_l + \frac{d}{dt}\varphi(t)$. For $\frac{d}{dt}\varphi(t) = f(t)$ the carrier frequency varies with the delay time and the corresponding pulse is said to be frequency modulated or chirped. The laser pulse is up or positively (down or

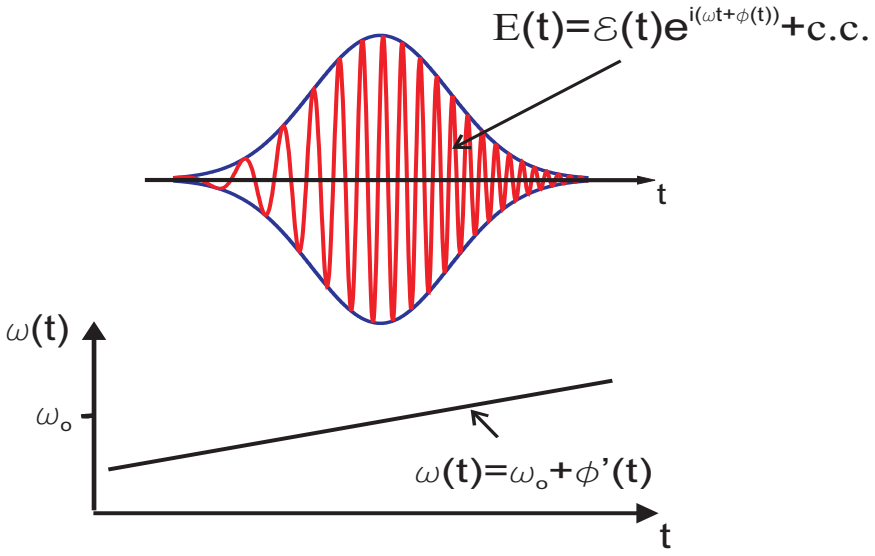

Fig. 1. An optical pulse with a positive linear chirp. The instantaneous frequency $\omega(t)$ changes linearly with the delay time.

negatively) chirped if $\frac{d^2}{dt^2}\varphi(t) > (<)0$.

The complex spectrum of the field strength $E(\omega)$ is defined through the Fourier transform of the time domain electric field

$$E(\omega) = |E(\omega)|e^{i\phi(\omega)} = \int_{-\infty}^{\infty} E(t)e^{-i\omega t}dt, \tag{2.2}$$

where $\phi(\omega)$ is the phase of the pulse in the frequency domain. $E(t)$ and $E(\omega)$ represent evolution of the electric field of the pulse in time and frequency domains respectively. Since these representations are not independent and are related through the Fourier transform, there is a fundamental relationship between the time duration of the pulse $\triangle t$ and the frequency bandwidth $\triangle\nu$

$$\triangle\nu \triangle t \geq c_B, \tag{2.3}$$

where c_B is a numerical constant value which depends on the shape of the pulse. It follows from this relationship, that generation of short pulses requires large gain

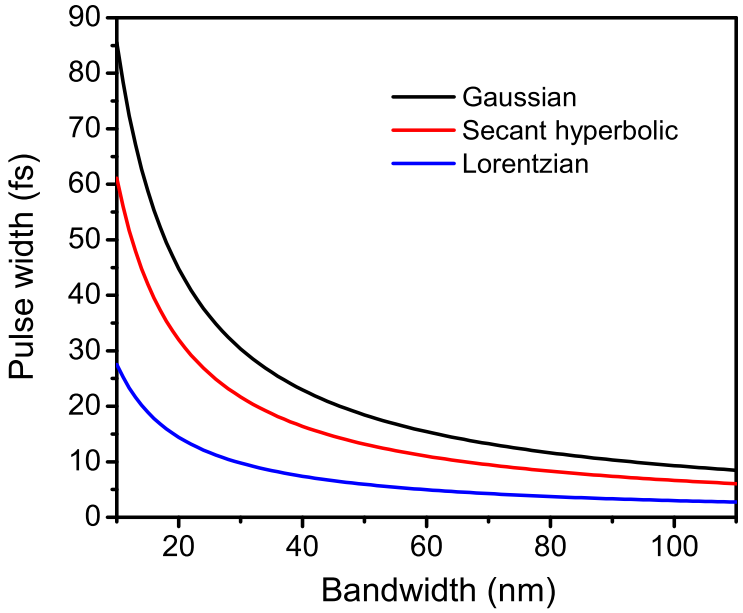

Fig. 2. Time duration of a transform-limited pulse versus the pulse bandwidth for Gaussian (black line), Secant Hyperbolic (red line), and Lorentzian (blue line) pulse shapes.

bandwidth of the lasing medium (Fig. 2). For a wavepacket of a given spectral width $\triangle\lambda$(nm), at the central wavelength λ, the minimum duration of the pulse is

$$\triangle t \geq \frac{c_B \lambda^2}{c \triangle \lambda}. \tag{2.4}$$

The equality in the above equation (so called transform-limited pulse) holds only when the spectral phase $\phi(\omega)$ is a linear function of frequency. This can be rarely achieved in the real world as the phase of an ultrashort laser pulse becomes distorted during propagation in a dispersive medium, additional spatial dispersion is acquired on gratings and prisms, etc. Assuming that the phase varies slowly with the frequency,

it can be expanded in the Taylor series around the central frequency of the pulse ω_0

$$\phi(\omega) = \sum_{n=0}^{\infty} \frac{1}{n!} \frac{d^n \phi(\omega_0)}{d\omega^n} (\omega - \omega_0)^n. \tag{2.5}$$

The first term in the expansion is related to the phase of the carrier wave under the envelope. The term linear in frequency describes the delay of the pulse as a whole (group delay). The quadratic term, which describes the linear group velocity dispersion (GVD), usually contributes the most to the ultrashort laser pulse broadening. It can be thought of as a distortion where the delay of a spectral component of the laser pulse is proportional to the offset of its frequency from the central frequency ω_0. The higher order terms are related to the higher order distortion of the laser pulse.

2. Kerr-lens mode-locking

Unlike a narrow-bandwidth laser where usually only one cavity mode is selected for CW operation, a femtosecond laser supports many longitudinal modes. In the free-running regime all the modes oscillate inside the cavity with random phases, which results in quasi-CW operation. For pulsed operation the phases of all the oscillating modes need to be synchronized (mode-locked). The mode-locking will result in a periodic constructive interference of the locked modes yielding at the output of the laser a train of short and intense laser pulses. A number of mode-locking techniques have been applied for femtosecond pulse generation including active, passive, and Kerr-lens modelocking. The later is based on the nonlinear Kerr-lens effect and is widely used in Ti:Sapphire lasers. This technique is also used in our oscillator.

Consider an intense laser beam with Gaussian intensity profile incident on a nonlinear medium (Fig. 3). In a strong laser field the index of refraction of the

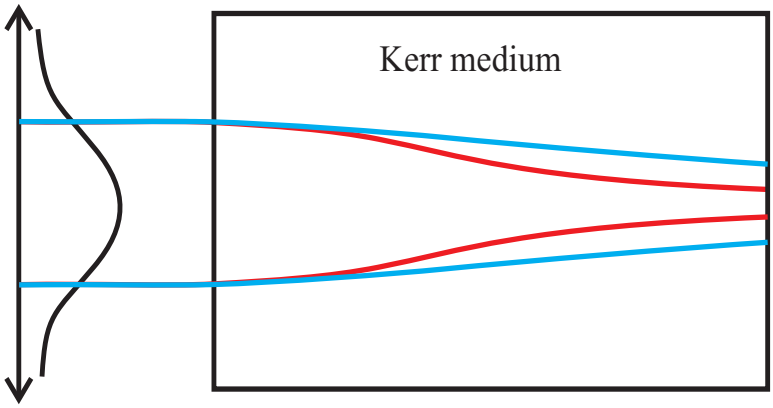

Fig. 3. Kerr-lensing effect. Effect of the Kerr self-lensing on a pulsed (red) and cw (blue) laser beams of the same average power propagating in a nonlinear Kerr medium. The pulsed laser light has higher intensity and correspondingly stronger self-lensing effect than the CW beam.

medium becomes a function of the field intensity and can be written in the form

$$n(r) = n_o + \frac{1}{2} n_2 I(r), \tag{2.6}$$

where n_o is the normal refractive index of the medium and n_2 is the nonlinear refractive index that describes the nonlinear effect of the laser field on the refractive index. For positive values of n_2 the refractive index is maximum at the center of the beam and gradually decreases to the edge. This refractive index change will result in focusing of the laser beam as it propagates inside the nonlinear material. The higher is the intensity of the laser beam the stronger is the self-lensing effect. The focusing of the beam inside the material will continue until it is equilibrated by the linear diffraction.

To efficiently utilize the Kerr-lensing effect, the cavity modes are focused inside the Ti:Sapphire crystal. If the cavity is optimized for the presence of the Kerr-lens, then pulsed operation of the laser, in which the intensity is higher and the self-lensing effect is stronger, will be favored over quasi-CW operation. Often in older designs an

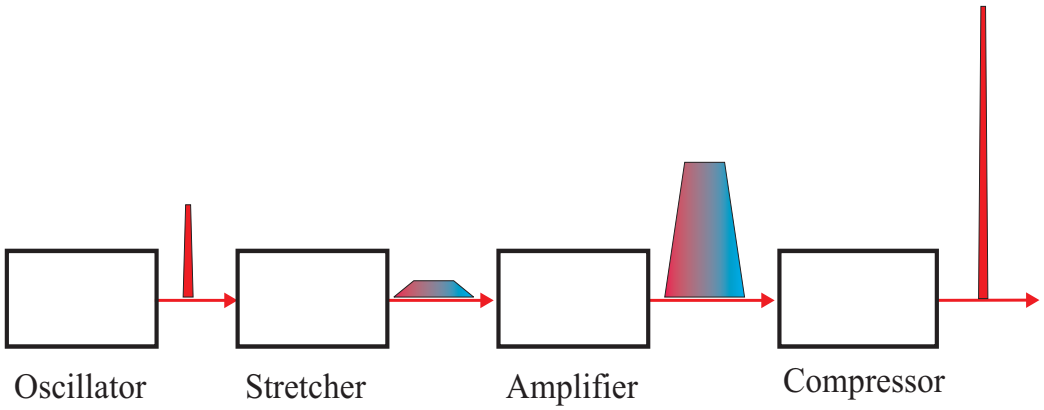

Fig. 4. Principle of a CPA process.

aperture was placed inside the cavity so that the cw radiation has higher losses than the pulses (hard aperture method). In the soft aperture method, the pump beam is focused into a narrow region of the crystal, so that the locked pulses have better overlap with the pumped area than these modes that are not locked.

3. Chirped Pulse Amplification (CPA)

The output of a typical Ti:Sapphire femtosecond oscillator is a train of pulses with a repetition rate of about hundred MHz with a pulse energy of about several nanojoules. To obtain femtosecond pulses in the millijoules energy range, the output of the oscillator needs to be amplified. One of the main problems in producing short and high energy optical pulses is that their high intensity ($\sim 10^{11}$ W cm^{-2}) can easily exceed the damage threshold of crystalline Ti:Sapphire ($\sim 10^{10}$ W cm^{-2} [19]). To avoid the damage of the active medium, the peak intensity needs to be reduced. This is achieved by the Chirped Pulse Amplification (CPA) technique which has been applied for amplification of the ultrashort laser pulses [20]. The principle of this technique is illustrated in Fig 4. First, the pulse from the oscillator is temporally stretched inside a stretcher by separating in time its frequency components. Then this pulse is directed

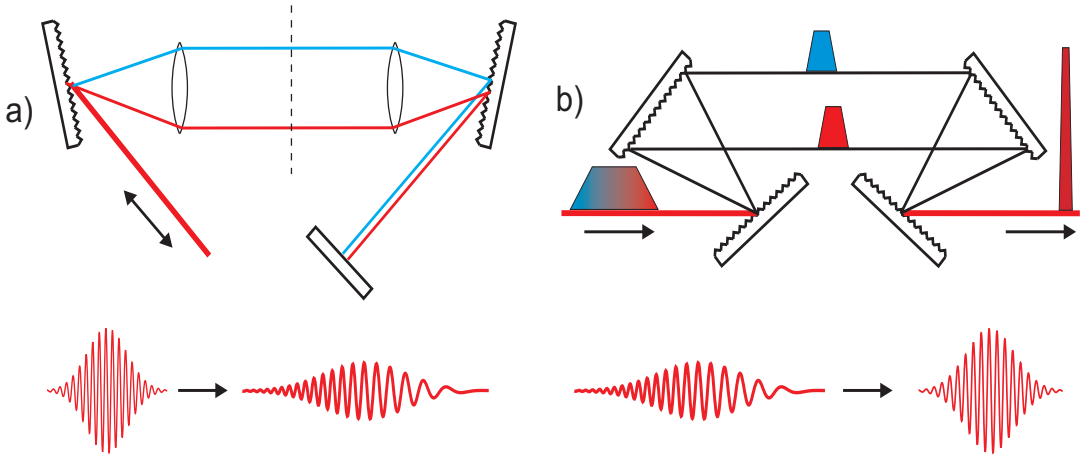

Fig. 5. Schematic of the grating stretcher a) and compressor b).

into the amplifier regenerative cavity, where it travels back and forth several times, being amplified each time. Finally, the amplified pulse is recompressed by putting its spectral components back together in a grating compressor. This technique allows one to produce short pulses of rather high intensity.

A typical stretcher is a combination of gratings and lenses (or mirrors), arranged in such a way that it has a positive GVD (Fig. 5 a)). The spectral components with shorter wavelengths travel longer optical distance than the spectral components with longer wavelengths. This results in spreading of the spectral components in time in a pre-determined manner. In a typical CPA system, the seed pulses are stretched by a factor of $10^2 - 10^4$. To compensate a positive GVD introduced to the laser pulse in the stretcher and the amplifier cavity, a grating compressor with a negative GVD is used. Opposite to the stretcher, the spectral components with longer wavelengths travel longer optical distance than the spectral components with shorter wavelengths (Fig. 5 b)). It should be noted that the amplified pulse is always longer then the seed pulse because in the amplifier cavity the optical pulse acquire also high order phase distortions that cannot be completely compensated by the compressor. Also during

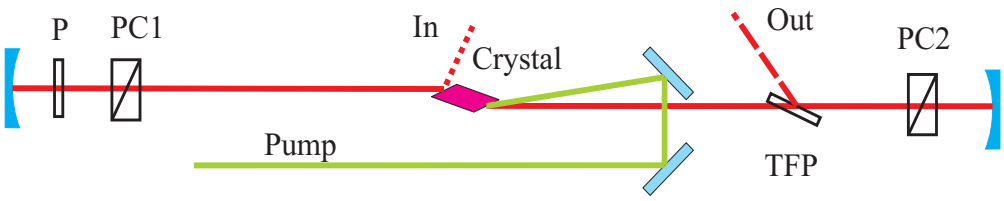

Fig. 6. Regenerative cavity.

the amplification process, the spectral width of the laser pulse is reduced due to gain narrowing.

After the stretcher, the seed pulses can be amplified using the regenerative amplification technique. The principal of regenerative amplification is illustrated in Fig. 6. The repetition rate of a typical oscillator is about a 100 MHz. Usually an amplifier is pumped by a laser source working at a repetition rate of several kHz, which means that only a small part of all pulses in the output train of the oscillator will be picked out and amplified. A selected seed pulse is let inside the cavity at the time when the pump pulse has just passed through the crystal. The pulse is kept inside the cavity until the gain is saturated, and after that it is let out of the cavity. For this purpose a fast optical switch with a response time in the nanosecond range is needed. For linearly polarized light a combination of the Pockels Cell and a broadband polarization analyzer can be used. The Pockels cell working principle is based on the electro-optic effect, i.e. a change of the refractive index of the material under application of an electric field. A birefringent crystal can act as a quaterwave plate or as a halfwave plate, depending on the applied voltage.

4. Second Harmonic Generation (SHG)

In our experiment it was desirable to have femtosecond laser pulses at the wavelength other then that available from the output of a Ti:Sapphire amplifier. Therefore fre-

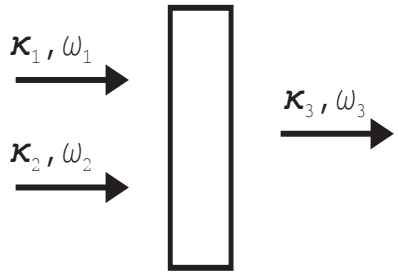

Fig. 7. Schematic of a sum-frequency mixing process.

quency doubling of the optical radiation in a nonlinear optical crystal was used. Its principle is based on the nonlinear response of matter to an intense electrical field. The second harmonic of the output of the amplifier radiation, generated in a BBO nonlinear crystal, was used as a probe in our experiments.

The macroscopic polarization $\mathbf{P}$ induced in the nonlinear optical medium by an electric field $\mathbf{E}$ can be presented as an expansion in a power series on the electric field

$$\mathbf{P} = \chi^{(1)}\mathbf{E} + \chi^{(2)}\mathbf{EE} + \chi^{(3)}\mathbf{EEE} + ..., \tag{2.7}$$

where the coefficients $\chi^{(i)}$ are the material succeptibilities. The first term describes the linear case. The term quadratic in the electric field is responsible for a variety of three-wave mixing processes such as optical parametric generation, frequency sum and frequency difference mixing, second harmonic generation. The higher order terms describe the higher order nonlinear processes.

In a sum frequency mixing two photons with frequencies ω_1 and ω_2 mix in a medium with high second order succeptibility $\chi^{(2)}$ resulting in a single photon of the frequency ω_3 (Fig. 7). The energy and the momentum conservation conditions for this process are:

$$\hbar\omega_1 + \hbar\omega_2 = \hbar\omega_3, \tag{2.8}$$

$$\mathbf{k}_1 + \mathbf{k}_2 = \mathbf{k}_3. \tag{2.9}$$

For the second harmonic generation (SHG) process, which is the degenerate case of the sum frequency mixing, these conditions reduce to:

$$\frac{n_{2\omega}}{\lambda_{2\omega}} = \frac{2n_{\omega}}{\lambda_{\omega}}, \tag{2.10}$$

where n_{ω} and $n_{2\omega}$ are the refractive indeces of the material at the frequencies ω and 2ω. Here it was assumed that the fundamental and the second harmonic beams are collinear. This equation coincides with the "phase matching" condition. In a normal medium with the dispersion $n \sim \frac{1}{\lambda}$ this condition cannot be satisfied. The phase matching can be achieved in a birefringent crystal, with the polarization of the fundamental and the second harmonic perpendicular to each other. For efficient second harmonic generation the phase mismatch $\triangle k = k_{2\omega} - 2k_{\omega}$ needs to be sufficiently small so that $\triangle kl \leq 1$, where l is the thickness of the SHG crystal.

5. Femtosecond pulse characterization

Because the duration of a femtosecond laser pulse is shorter than the time resolution of any modern electronics, there is no direct way of measuring its time duration or intensity profile. However, this can be done optically, and one of the most widely used methods for characterization of femtosecond pulses is the autocorrelation technique. In this method a nonlinear medium, usually a SHG crystal, is used to obtain an autocorrelation function of the laser pulse. In a SHG non-collinear autocorrelator the incident laser pulse of the fundamental frequency ω is split in two pulses by a 50/50 beam-splitter (Fig. 8). The two replicas of the pulse are overlapped in space and time in a SHG crystal under phase-matching geometry. The intensity of the second harmonic $I_{2\omega}(t)$ generated inside the crystal is given by

$$I_{2\omega}(t) \sim I(t)I(t-\tau), \tag{2.11}$$

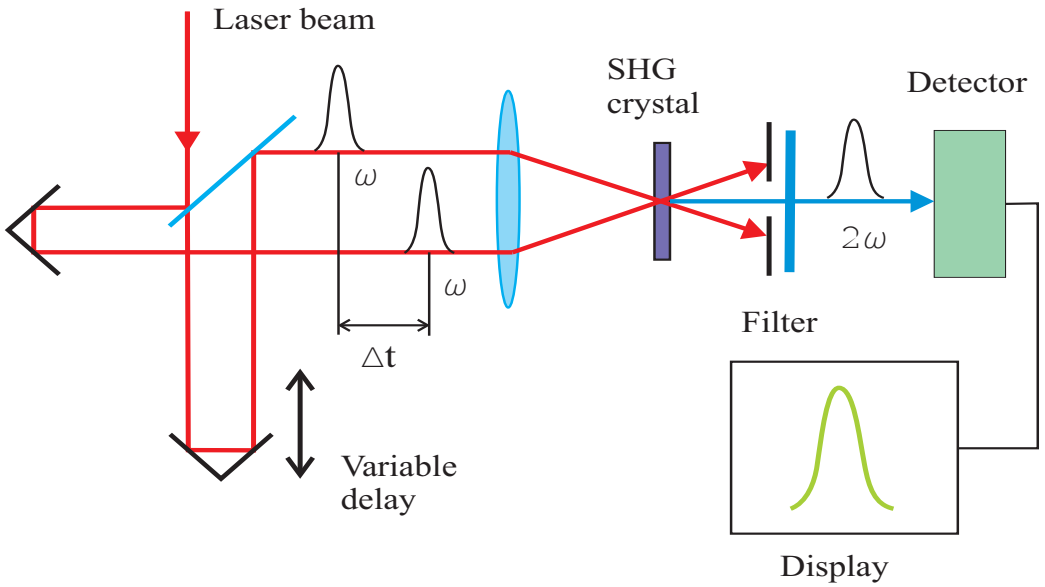

Fig. 8. Schematic diagram of a SHG non-collinear autocorrelator. The laser pulse is split by a 50/50 beam splitter into two replica parts and then recombined in a nonlinear mixing crystal after the two parts have experienced a known relative time delay.

where τ is the delay between the two pulses. The second order non-collinear intensity autocorrelation function is defined as

$$A_{ac}(\tau) = \frac{\int I(t)I(t-\tau)dt}{\int I^2(t)dt}. \tag{2.12}$$

Because different pulse shapes can have similar autocorrelation traces the autocorrelation function gives incomplete information about the shape of the laser pulse. To obtain the duration of the pulse a particular pulse shape needs to be assumed first. Then the Full Width at Half Maximum (FWHM) of the autocorrelation trace τ_a can be related to that of the intensity profile of the laser pulse τ_p. The ratios τ_p/τ_a for the most generally used pulse shapes are presented in Table I.

In the cross-correlation technique, a reference pulse of a known shape $I_r(t)$ is used in order to determine the temporal profile of the unknown pulse $I_s(t)$. The

Table I. Second-order correlation and time-bandwidth products for various pulse-shape models. Here τ_p is pulse width (FWHM), τ_G is autocorrelation width (FWHM) and $\triangle\nu$ is spectral width

Pulse shape	I(t)	$\triangle\nu\tau_p$	$\frac{\tau_p}{\tau_a}$
Gaussian	$Exp(-\frac{4ln2t^2}{\tau_p^2})$	0.4413	0.7071
Secant hyperbolic	$sech^2(\frac{1.76t}{\tau_p})$	0.315	0.6482
Lorentzian	$1/(1+\frac{2t}{\tau_p})^2$	0.2206	0.5000

intensity cross-correlation function can be written as

$$A_{cc}(\tau) = \int I_r(t) I_s(t-\tau) dt. \tag{2.13}$$

B. Laser System

1. Femtosecond oscillator

The source of the femtosecond pulses in our laser system is a Kerr-lens mode-locked Ti:Sapphire oscillator (Kapteyn-Murnane Labs, KML TS). The outline of the oscillator is presented in Fig 9. The active medium is a Ti:Sapphire crystal cut at the Brewster angle to minimize the losses. The oscillator is pumped by the output of a diode-pumped intracavity-doubled Nd:YAG laser (Spectra Physics, Millennia V) with a power of about 5 W and a wavelength of 532 nm. The pump beam is focused inside the crystal collinearly with the laser axis. To achieve the Kerr-lens effect two concave mirrors are placed forming a telescope with the crystal in the focal plane. A combination of two prisms P1 and P2 is used to compensate for the dispersion introduced in the crystal. The output of the oscillator is a train of pulses at a repetition rate of 87 MHz, pulse energy about 5 nJ, and pulse duration of about 35 fs. The

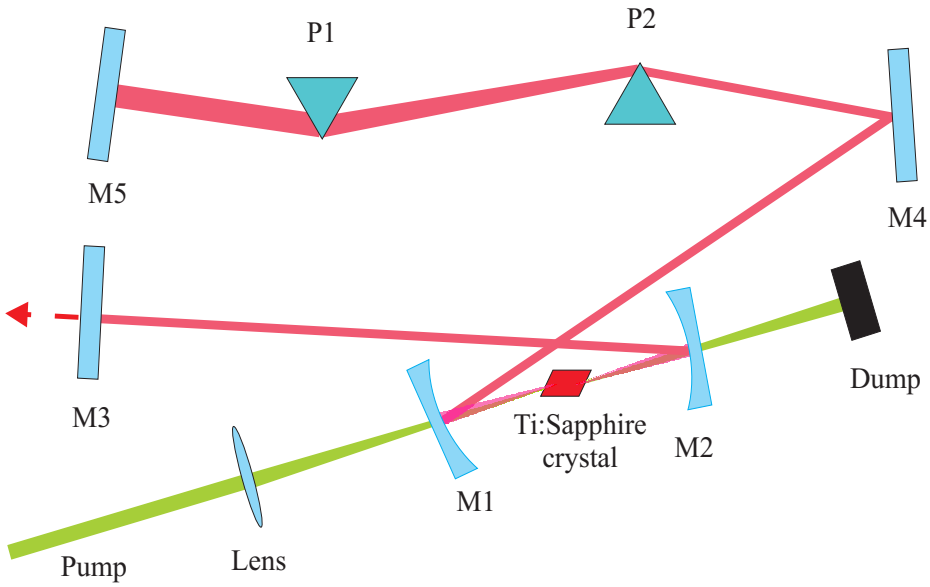

Fig. 9. The outline of the Ti:Sapphire femtosecond oscillator. M1, M2, M3, M4, M5 are the cavity mirrors, where M3 is at the same time the output coupler. The group velocity dispersion experienced by the laser pulse traveling inside the crystal is compensated by a pair of prisms P1 and P2.

central wavelength of the oscillator can be tuned in the range 780-830 nm. A typical autocorrelation trace of the output of the oscillator is shown in Fig 10.

2. Regenerative amplifier

The output of the oscillator is amplified in a regenerative Ti:Sapphire amplifier (Spectra Physics, Spitfire). The schematic diagram of the amplifier is presented in Fig 11. It consists of three main parts: stretcher, regenerative cavity, and compressor. The seed pulses first are expanded in time in a grating stretcher. The amplifier is pumped by a Q-Switched Nd:YAG laser (Spectra-Physics, Merlin) at a repetition rate of 1 kHz. A photodiode PD is placed behind one of the cavity mirrors so the buildup trace can be monitored on a oscilloscope. The output of the amplifier is a train of pulses with a repetition rate of 1kHz, pulse energy 0.75 μJ, and pulse duration of

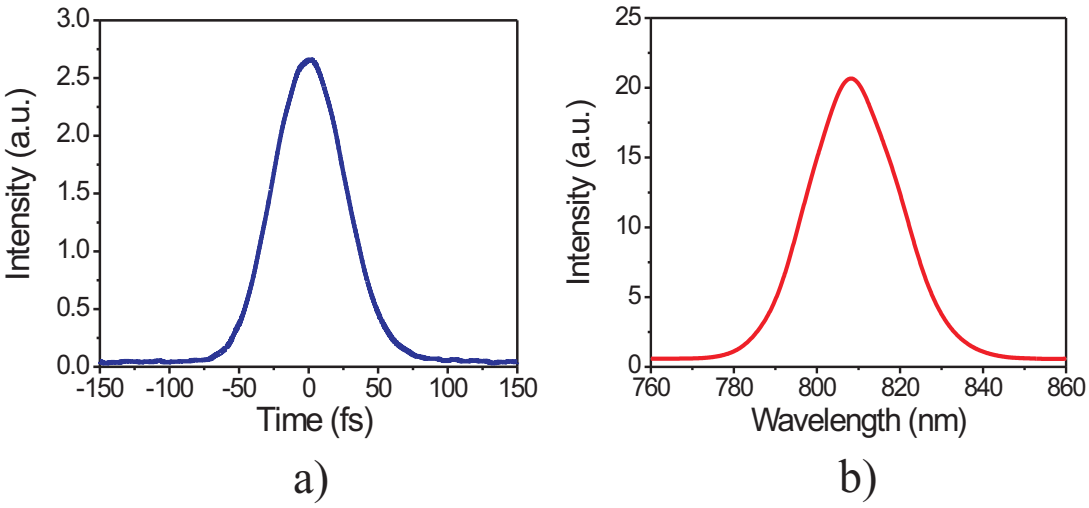

Fig. 10. An intensity autocorrelation trace a) and spectrum b) of the output of the oscillator. The trace was measured by a commercial auto correlator (APE, Mini) in background-free non-collinear mode.

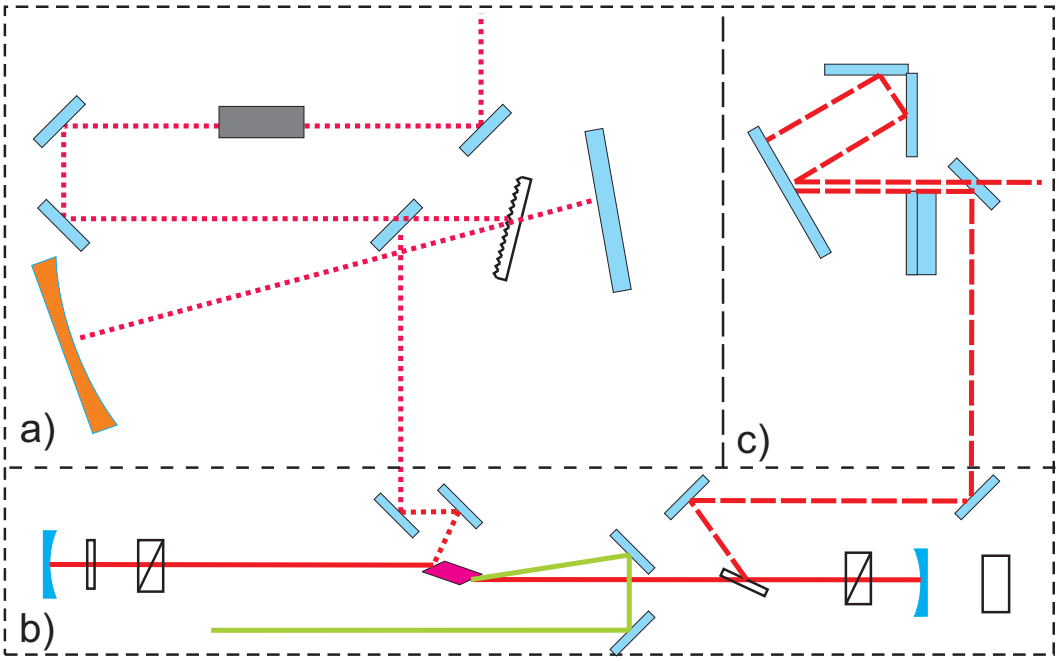

Fig. 11. The outline of the Ti:Sapphire regenerative amplifier. The three main parts are the stretcher a), regenerative cavity b), and the compressor c).

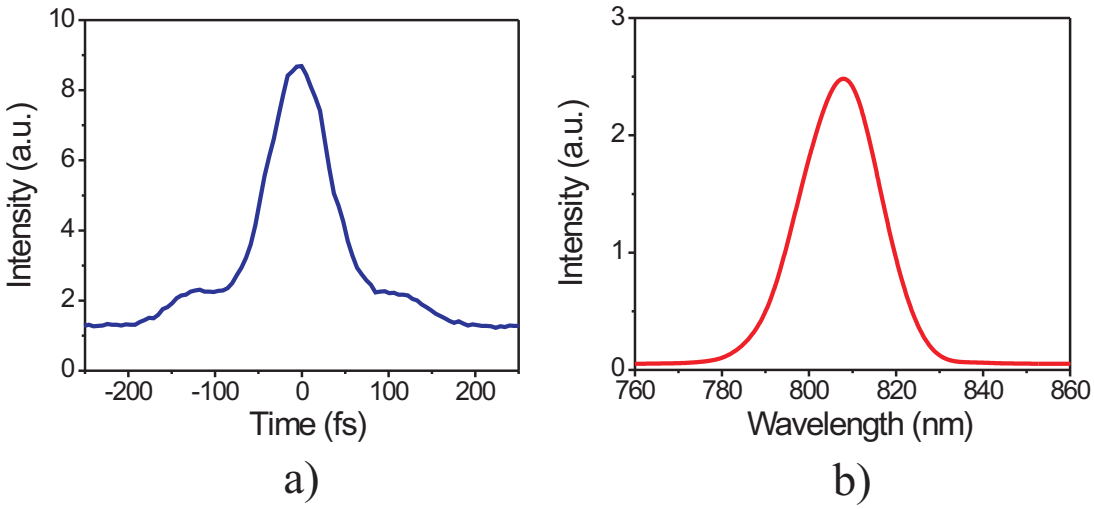

Fig. 12. An intensity autocorrelation trace a) and spectrum b) of the output of the amplifier. The output of the laser was split by a beam splitter and the two laser pulses were overlapped on a second harmonic generation crystal. The generated second harmonic radiation was detected by a photodiode.

about 50 fs. The autocorrelation signal of the output of the amplifier is presented in Fig 12.

C. Transient Transmission Part

Fig. 13 depicts the experimental arrangement for the pump-probe spectroscopy. The pump and probe pulses were obtained by splitting the output of the Ti:Sapphire regenerative amplifier by a 10/90 beam splitter into two parts. The 90% part was used as a source of pump pulses. The pump beam was modulated by a mechanical chopper, which was synchronized with the laser, at a frequency of half the repetition rate of the laser. The intensity of the pump beam was adjusted by a neutral density filter, and the beam was directed into the pump delay arm. The 10% beam was directed to a SHG BBO crystal and the generated blue light was used as a probe. It was directed into the probe delay line with a computer controlled motorized translation stage.

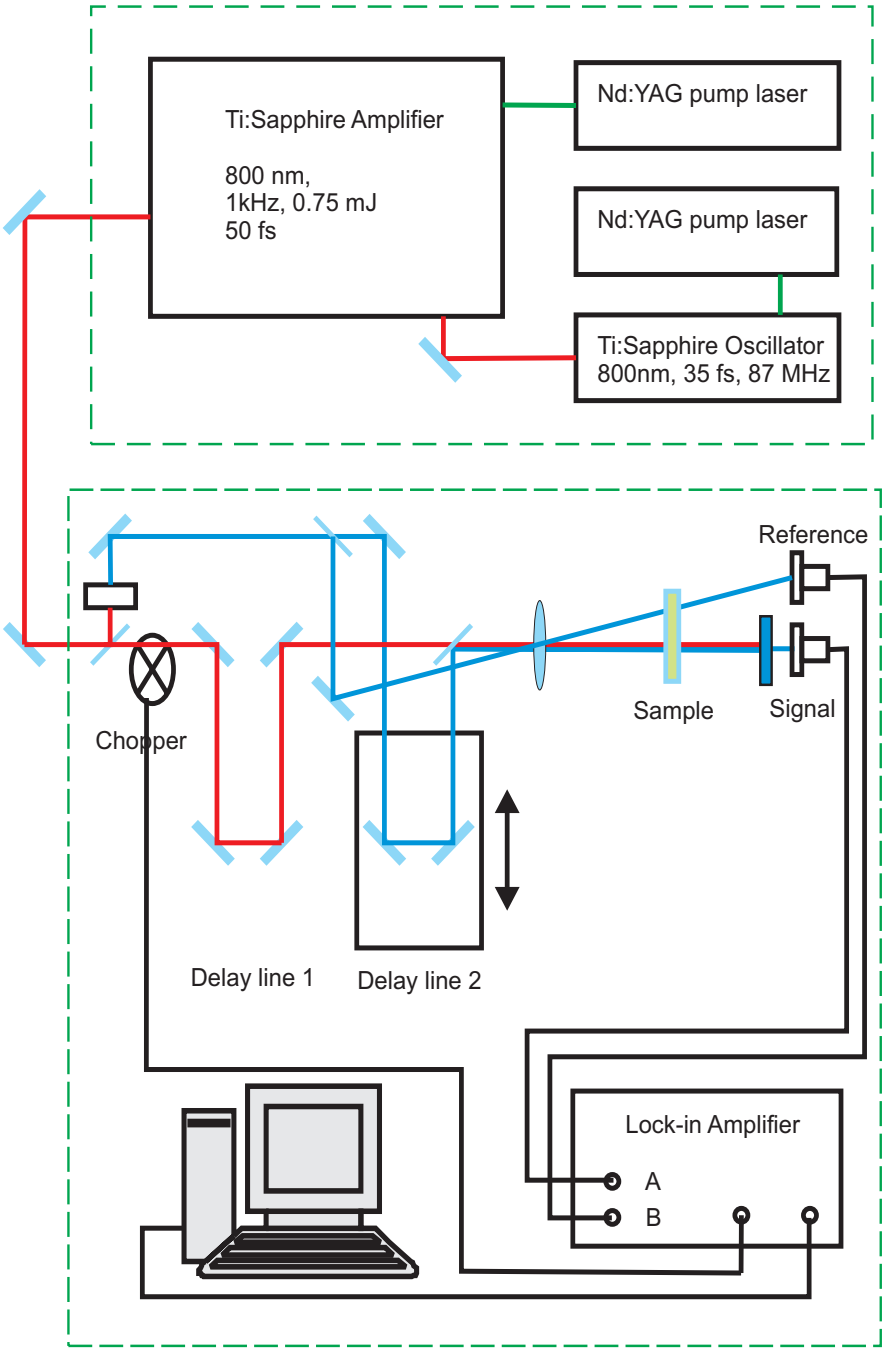

Fig. 13. Experimental setup diagram.

Part of the probe beam was taken off by a beam splitter and used as a reference. The reference beam was used to compensate for the fluctuations of the laser intensity and helped to improve the signal-to-noise ratio. The pump and probe beams were focused by a lens of focal length 150 mm onto a glass cuvette containing the sample. The optical path length of the cuvette was 2mm. To optimize the signal level, the concentration of the sample was adjusted for $\sim$50% transmission of the probe beam. After traversing the sample the probe and the reference beams were detected by matched large area photodiodes (UDT-PIN 10D). Schott filters (BG12) were put in front of the photodiodes to block the transmitted pump beam. The outputs of the photodiodes were connected to the two channels of a lock-in amplifier and the difference of the signals from the probe and reference photodiodes was amplified. The lock-in amplifier was referenced to the chopper. The output of the lock-in amplifier was proportional to the change in the sample transmission induced by the pump beam. By varying the delay between the probe and the pump pulses the transient response of the sample was measured. The output of the lock-in amplifier was connected to a data-acquisition card and the experimental data were stored in a computer.

CHAPTER III

COHERENT ACOUSTIC VIBRATIONS IN NANOPARTICLES AND NANOWIRES

Recent advances in fabrication of new nanomaterials have stimulated studies of their properties. At the nanoscale, materials have properties different from those of the molecules they are made of and bulk matter. Control of these properties via shape and size of the nanomaterial is both of fundamental and technological interest.

Metal nanometer-size particles have attracted attention in recent years. This interest is driven by the desire to understand the properties of these materials, and possible applications, such as in advanced composite materials, optical limiting devices, application to selective heating of condensed matter and biological systems. The femtosecond pump-probe technique has been applied to studies of the elastic, thermodynamic and optical properties of metal nanoparticles.

The mechanical properties of nanostructures can differ significantly from those of the bulk material. For example, the values of the Young's modulus of carbon nanotubes are larger than those of the corresponding bulk matter [21, 22]. Min Hu *et. al* [23] studied the acoustic response of Au nanorods of diameters 10-20 nm and aspect ratios 2-5 prepared by the seed mediated growth technique. This method yields high quality nanorods with five-folded structure. They found that the elastic constants of these particles are about 20% smaller than those of the bulk material. The structure of the metal nanoparticle depends on the preparation method used. It was found that for the metal nanowires prepared by electrodeposition technique the crystallinity of the sample depends on the electrodeposition potential [24].

The behavior of nanoparticles under strong laser excitation has been a subject of theoretical modeling and experimental studies. In the experiments with the Au

spheres excited with intense laser pulses softening of the lattice was observed, although no abrupt increase in the period of acoustic oscillation that would indicate the melting of the particles, was found [25]. Molecular dynamics simulations of nanoclusters with numbers of atoms from 300 up to 1500 have been performed. It was found that for smaller particles there is essentially no coexistence of the two phases, whereas in the larger particles the molten and solid phases can be present in the particle at the same time.

In the present work, the acoustic properties of Ag spherical nanoparticle and Ag and Bi nanowires of high aspect ratio were studied with a femtosecond pump-probe technique. The Ag spherical nanoparticle were prepared by a wet chemistry method, the Ag and Bi nanowires were produced by the template-assisted electrodeposition technique. The transient response of the Ag spherical particles in aqueous solution was measured in the transmission geometry. For the nanowires, the probe beam light scattered from the sample was detected. The information on the period of the acoustic vibrations, obtained from the time-domain measurements with low intensity pump pulses, together with the information about the size of the particles were used to determine the elastic constants of the material. Also changes in the acoustical response of the Ag nanowires under high intensity laser excitation were studied.

A. Optical Properties of Metal Spheres and Rods

The reduction of the object size to the nanoscale leads also to changes of the optical properties. For small metal particles, the absorption and scattering peaks due to the surface plasmon resonance can appear in the optical region [26]. The position, intensity, and width of the peaks depend on the shape and size of the particles and on the dielectric constant of the surrounding medium [27]. For very small particles of

sizes less than about 5 nm the theoretical description is best based on the quantum mechanical approach, for larger particles, which were studied in the present work, the classical electromagnetic theory (e.g., Mie's theory for small spheres and Gan's theory for ellipsoids) is adequate.

1. Dielectric function of a metal particle

The linear response of metals to an electromagnetic field is described by the dielectric function $\varepsilon(\omega)$. For noble metals, both transitions within the conduction band and interband transitions from lower-lying bands into the conduction band contribute to the dielectric function.

In the Drude-Lorentz-Sommerfeld model, the response of the conduction electrons to the external field can be found by first considering the influence of the external field on one free electron alone. To obtain the macroscopic response, the single electron response is simply multiplied by the number of the electrons. The response of a free electron of mass m_e and charge e to an external electric field $\mathbf{E} = \mathbf{E_0}e^{-i\omega t}$ is described by the equation

$$m_e \frac{\partial^2 \mathbf{r}}{\partial t^2} + m_e \Gamma_0 \frac{\partial \mathbf{r}}{\partial t} = e\mathbf{E_0}e^{-i\omega t}, \tag{3.1}$$

where Γ denotes the phenomenological damping constant, which can be related to the electron mean free path l by $\Gamma_0 = v_F/l$. v_F is the Fermi velocity of the electrons. The solution of this equation gives the dipole moment $\mathbf{p} = e\mathbf{r_0}$ and the polarization $\mathbf{P} = n\mathbf{p}$, where n is the electron density. In an isotropic medium $\mathbf{P}$ is parallel to $\mathbf{E}$ and the dielectric function $\varepsilon(\omega)$ is $\varepsilon = 1 + P/(\varepsilon_0 E)$. Thus, the dielectric function $\varepsilon(\omega) = \varepsilon_1(\omega) + i\varepsilon_2(\omega)$ of a system of n free electrons per unit volume can be written

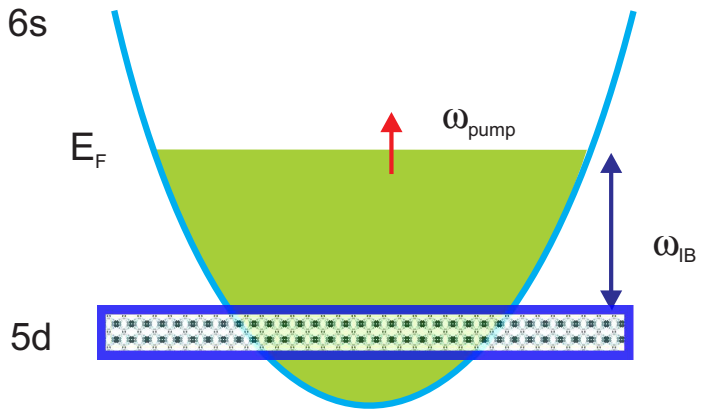

Fig. 14. Schematic band structure of silver. E_F is the Fermi energy level, $\hbar\omega_{IB}$ is the energy of the interband transitions from the d-band to the conduction band. The infrared pump beam excites electrons in the conduction band.

as

$$\varepsilon(\omega) = 1 - \frac{\omega_p^2}{\omega^2 + i\Gamma\omega} = 1 - \frac{\omega_p^2}{\omega^2 + \Gamma^2} + i\frac{\omega_p^2\Gamma}{\omega(\omega^2 + \Gamma^2)}, \tag{3.2}$$

where $\omega_p = (ne^2/\varepsilon_0 m_e)^{1/2}$ is the Drude plasma frequency. For small particles, when the size of the particle is smaller than the mean free path the relaxation constant Γ has additional contribution from the scattering of the electrons on the surface

$$\Gamma = \Gamma_0 + A\frac{v_F}{R}, \tag{3.3}$$

where R is the radius of the particle, V_F is the Fermi velocity of the electrons and Γ_0 is the bulk damping constant.

Electrons in the lower-lying bands also contribute to the dielectric function. The interband transitions give a complex contribution $\chi^{IB} = \chi_1^{IB} + i\chi_2^{IB}$ to the susceptibility. The diagram of the band structure of silver is shown in Fig. 14. In a noble metal like silver, the main contribution comes from the transitions from the d-band to the conduction band. Following Rosei *et al.* [28] the imaginary part of the interband

contribution can be written as

$$\varepsilon_2^{IB}(\omega,T) \propto \frac{1}{\omega^2}\int_0^\infty D(E,\omega)[1-n(E,T)]dE, \tag{3.4}$$

where $D(E,\omega)$ is the energy-distributed joint density of states, $n(E,T)$ is the Fermi distribution function, T is the temperature of the electrons. The real part of the interband succeptibility is obtained by the Kramers-Kronig relation

$$\varepsilon_1^{IB}(\omega,T) = \frac{2}{\pi}\int_0^\infty \frac{\omega'\varepsilon_2^{IB}(\omega',T)}{\omega'^2-\omega^2}d\omega'. \tag{3.5}$$

It should be noted that the interband part of the dielectric function is temperature dependent.

2. The Mie theory

In his paper published in 1908 [29], Mie obtained a rigorous solution of the absorption and scattering of an electromagnetic light wave by a homogeneous sphere. Mie used the same macroscopic frequency-dependent material dielectric constant as that of the bulk metal. The solution of this electromagnetic calculation with appropriate boundary conditions leads to a series of multipole oscillations for the extinction cross-section of the particle. The extinction cross-section σ_{ext} and scattering cross-section σ_{sca} are given by [30]

$$\sigma_{ext} = \frac{2\pi}{|k|^2}\sum_{L=1}^{\infty}(2L+1)Re(a_L+b_L) \tag{3.6}$$

$$\sigma_{sca} = \frac{2\pi}{|k|^2}\sum_{L=1}^{\infty}(2L+1)(|a_L|^2+|b_L|^2), \tag{3.7}$$

with

$$a_L = \frac{m\psi_L(mx)\psi_L'(x)-\psi_L'(mx)\psi_L(x)}{m\psi_L(mx)\eta_L'(x)-\psi_L'(mx)\eta_L(x)}, b_L = \frac{\psi_L(mx)\psi_L'(x)-m\psi_L'(mx)\psi_L(x)}{\psi_L(mx)\eta_L'(x)-m\psi_L'(mx)\eta_L(x)}.$$

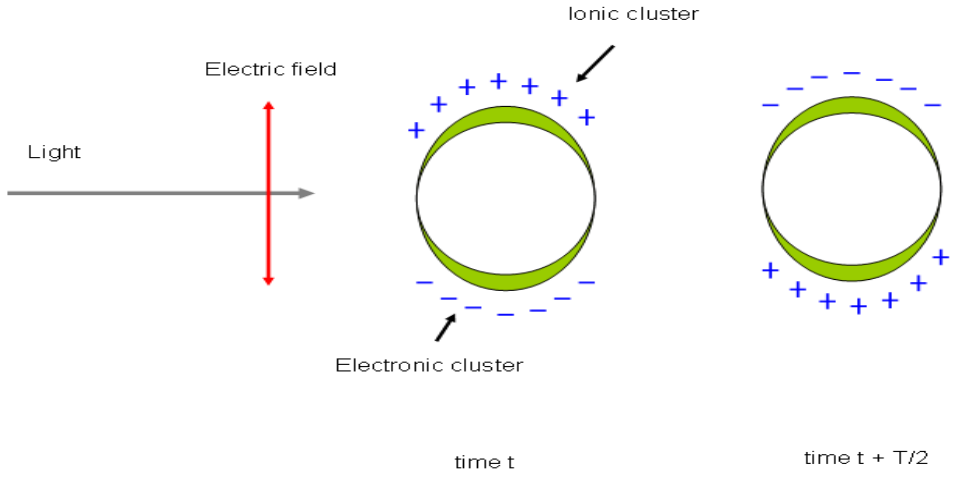

Fig. 15. Excitation of a dipolar surface plasmon by the electric field of a linearly polarized incident light wave of frequency $\nu = 1/T$.

Here, ψ_L and η_L are the Ricatti-Bessel cylindrical functions, $m = n/n_m$, in which n is the complex refractive index of the particle and n_m is the real refraction index of the surrounding medium. Also the variable $x = |\mathbf{k}|r$ was introduced, where r is the radius of a nanoparticle and $\mathbf{k}$ is the wave-vector of the incident light wave. The prime notation indicates differentiation with respect to the argument in parentheses.

For nanoparticles much smaller than the wavelength of light ($r << \lambda$, or roughly $2r < \lambda_{max}/10$) only the dipole oscillation contributes significantly to the extinction cross-section. The Mie theory then reduces to the following relationship (dipole approximation):

$$\sigma_{ext}(\omega) = 9\frac{\omega}{c}\varepsilon_m^{3/2}V\frac{\varepsilon_2(\omega)}{[\varepsilon_1(\omega)+2\varepsilon_m]^2+\varepsilon_2(\omega)^2}, \tag{3.8}$$

where V is the particle volume, ω is the angular frequency of the exciting light, c is the speed of light, and ε_m and $\varepsilon(\omega) = \varepsilon_1(\omega) + i\varepsilon_2(\omega)$ are the dielectric functions of the surrounding medium and of the nanoparticle itself respectively. The resonance

occurs when $\varepsilon_1(\omega) = -2\varepsilon_m$ if ε_2 is weakly dependent on ω.

Figure 15 shows how one can picture the creation of a dipole surface plasmon oscillation in a simple manner. The electric field of the incoming light wave induces a polarization of the conduction electrons with respect to the much heavier ionic core of a spherical nanoparticle. The net charge difference occurs at the nanoparticle boundaries which in turn acts as a restoring force. In this manner a dipolar oscillation with a period T is created.

3. The Gans model

The optical properties of a nanoparticle depend on its size and the environment, however the particle shape can have even stronger influence on its optical properties. Unfortunately, it is not possible to obtain an analytical solution for a particle of an arbitrary shape. In his model Gans extended the Mie theory to elongated ellipsoids assuming the size of the particles to be smaller than the wavelength of the incident light [31]. He predicted that the plasmon band of a sphere will split into two bands as the sphere is extended along one direction. The longitudinal band corresponds to the polarization along the long axis of the ellipsoid, and the transverse band corresponds to the polarization in the direction perpendicular to the long axis. For a sample of randomly oriented rods of the radius a and the length l the extinction cross-section can be written as [32]:

$$\sigma_{ext}(\omega) = \frac{\omega}{3c}\varepsilon_m^{3/2} V \sum_j \frac{(1/P_j^2)\varepsilon_2(\omega)}{[\varepsilon_1(\omega) + ((1-P_j)/P_j)\varepsilon_m]^2 + \varepsilon_2^2(\omega)}, \tag{3.9}$$

where P_j are the depolarization factors along the axes A, B, and C of the nanorod with A>B=C.

$$P_A = \frac{1-e^2}{e^2}\frac{1}{2e} ln(\frac{1+e}{1-e}) - 1, \tag{3.10}$$

$$P_B = P_C = \frac{1 - P_A}{2}, \tag{3.11}$$

and

$$e = (1 - (\frac{B}{A})^2)^{1/2}. \tag{3.12}$$

This expression for the cross-section was derived assuming a small volume fraction of the ellipsoids. For a large volume fraction, when the distances between the particles become comparable to the particle size and the wavelength of the incident light the problem of calculating the optical properties of the nanoparticle system becomes much more complicated.

B. Vibrational Modes of Spheres and Long Rods

1. Vibrational modes of a homogeneous elastic sphere

The acoustic modes of a homogeneous free elastic sphere were first investigated by H. Lamb[14]. Later the model was extended to a sphere embedded in an infinite elastic matrix[33, 16]. In this model, the vibrational mode characteristics depend only on the density and elastic constants of the sphere and the surrounding medium. This approach can be applied to nanospheres of a typical size $R \geq 2nm$ and low-frequency modes with a spatial displacement distributed on a scale much larger than the interatomic distance.

The acoustic modes in a homogeneous elastic sphere embedded in an infinite elastic matrix can be described by a solution of the Navier equation with appropriate boundary conditions. The displacement vector inside and outside of the sphere can be written in the form $\mathbf{u}(\mathbf{r}, t) = \mathbf{u}(\mathbf{r})exp(-i\omega t)$+c.c. [34]. These vibrational eigenmodes are divided into two types. The first type is the spheroidal vibrations with a nonzero radial displacement component ($u_r \neq 0$). These modes are related to volume changes.

The second type are torsional vibrations with $u_r = 0$. These modes correspond to an oscillation without changes of volume. In the present experiments only vibrations with volume changes can be detected so only the spheroidal modes will be considered. The discussion will be limited further to the radial modes, i.e. fully isotropic modes, where only the radial part of the displacement is non-vanishing. These modes are characterized by an angular momentum number $l = 0$ and a radial solution number n. The frequency of these eigenmodes can be found by solving the following equation [34, 35]:

$$\xi_n cot(\xi_n) = 1 - \frac{\xi_n^2}{\eta} \frac{1 + i\xi_n/\alpha}{\xi_n^2 - 4\alpha^2\gamma^2(1 - 1/\eta\beta^2)(1 + i\xi_n/\alpha)}, \tag{3.13}$$

in which ξ_n is the normalized frequency and the different parameters are given by $\alpha = V_L^{(m)}/V_L^{(s)}$,$\beta = V_T^{(m)}/V_T^{(s)}$,$\gamma = V_T^{(m)}/V_L^{(s)}$,$\eta = \rho^{(m)}/\rho^{(s)}$, where $\rho^{(m)(s)}$, $V_L^{(m)(s)}$ and $V_T^{(m)(s)}$ are the density, the longitudinal and transverse sound velocities of the matrix and the sphere materials respectively. For weak coupling between the sphere and the matrix, i.e. when the mismatch between the acoustic impedances of the sphere and the surrounding media is large, the vibrational frequency is proportional to the real part of the normalized frequency

$$\omega_n = Re(\xi_n)\frac{V_L^{(s)}}{R}. \tag{3.14}$$

The transfer of the acoustic energy from the sphere to the matrix results in damping of the acoustic vibration of the sphere. The damping rate is proportional to the imaginary part of the normalized frequency

$$\gamma_n = Im(\xi_n)\frac{V_L^{(s)}}{R}. \tag{3.15}$$

For a sphere in water the real part of the normalized frequency only slightly differs from that of a free sphere. The imaginary part of the normalized frequency is very

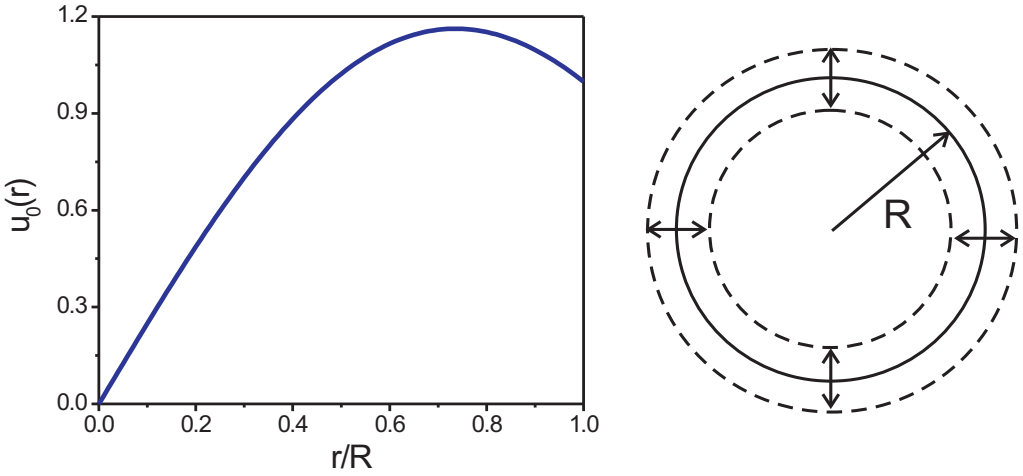

Fig. 16. The fundamental breathing mode displacement for a free sphere of radius R.

small because of the large mismatch in the acoustic impedance of silver ($\rho^{(Ag)}V_L^{(Ag)} \approx 38 \cdot 10^6$ kg m^{-2}s^{-1}) and water ($\rho^{(W)}V_L^{(W)} \approx 1.5 \cdot 10^6$ kg m^{-2}s^{-1}).

For the radial modes, the vibration is described only by the radial displacement and for a free sphere it is given by:

$$u_{0n} = \frac{B_{0n}}{y_n^2}(y_n cosy_n - siny_n), \tag{3.16}$$

where $y_n = \xi(0,n)r/R$. The fundamental breathing mode, i.e. the mode with the solution number n=0, is illustrated in Fig 16.

2. Vibrational modes of a long rod

The temporal response of a nanowire to excitation by a femtosecond laser pulse can be modeled by a linear elastic rod. Let us consider a free rod of length L and radius R irradiated by a short laser pulse. Energy transfer from the excited electron system to the lattice happens on the picosecond time scale, which is much shorter than the period of the fundamental acoustic mode of the nanoparticles studied in the

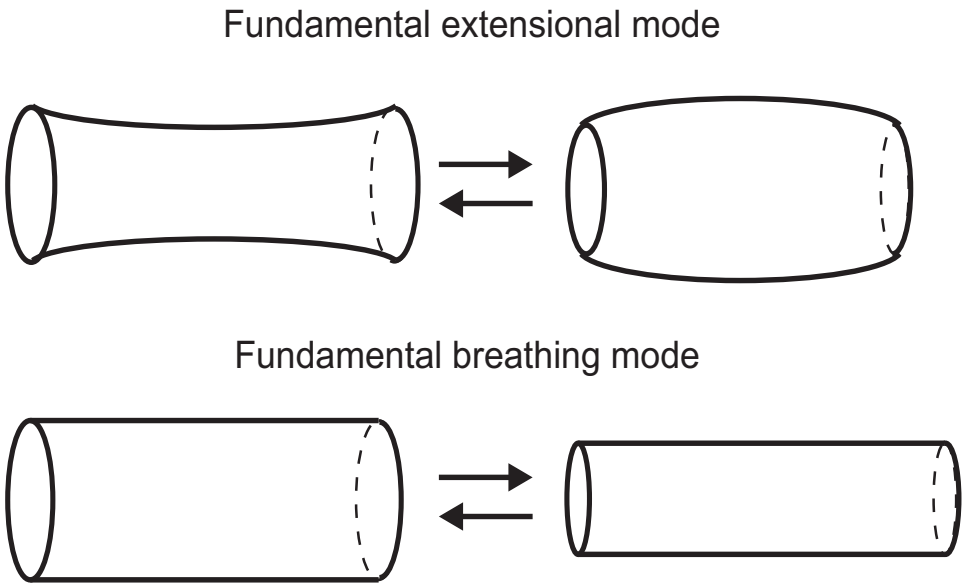

Fig. 17. The fundamental breathing and extensional modes of a long rod.

present work, so the excitation can be thought of as being instantaneous. In this approximation the excitation by a laser pulse can be modeled as a uniform strain applied to the rod at the initial moment of time. The aspect ratio of a rod is defined as the ratio of the length to the diameter of the rod. For rods with large aspect ratios ($L/R \gg 1$) two classes of modes are excited: the extensional modes and the breathing modes. The fundamental breathing and extensional modes are illustrated in Fig. 17. In the extensional mode, the increase in length is accompanied by contraction in the radial direction. This is the mode without change in volume. In the breathing mode the rod expands and contracts in the radial direction without change in length and this mode occurs with a change in the volume. The nanowires studied in the present experiments have rather large length (5-15 μm) which corresponds to a period of the extensional mode in the ns range. To detect these low frequency acoustic oscillations, delays of the probe pulse of about a meter would be needed, which is not very easy to implement experimentally and was not attempted. On the other hand the period

of the breathing mode vibrations is within the range of a hundred picosecond and is accessible with commercially available motorized translation stages. In this work, acoustic vibrations of the breathing mode were studied. For an elastic rod of high aspect ratio the frequency of the breathing mode is given by [23]

$$\omega_{br}^{(n)} = \frac{\tau_n}{R}\sqrt{\frac{E(1-\nu)}{\rho(1+\nu)(1-2\nu)}}, \tag{3.17}$$

where E is the bulk modulus, ν is the Poisson's ratio, ρ is the density of the material, and τ_n is the n-th root of the following equation

$$\tau J_0(\tau) = \frac{1-2\nu}{1-\nu} J_1(\tau). \tag{3.18}$$

C. Coherent Acoustic Vibrations in Silver Nanospheres

1. Sample preparation and characterization

The aqueous solutions of silver nanoparticles used in the experiments were produced by the conventional reduction method found in the literature [36, 37]. This method allows to produce nanoparticles with a relatively narrow size distribution. Variations in temperature and concentration can produce nanoparticles in the range from 10 to about 100 nm. In the following two typical examples are described.

The Ag particles of smaller size ("small particles") were produced by slowly adding 33 mL of a 1×10^{-3} M AgNO3 solution to 100 mL of a 2×10^{-3} M NaBH4 solution at 0^oC.

The Ag particles of larger size ("large particles")were prepared by the conventional reduction method by reducing of AgNO3 in water with sodium citrate at near-boiling temperature. 95 mL of a 1×10^{-3} M AgNO3 solution was heated to boiling temperature, and then 5 mL of a 1% sodium citrate solution was rapidly added.

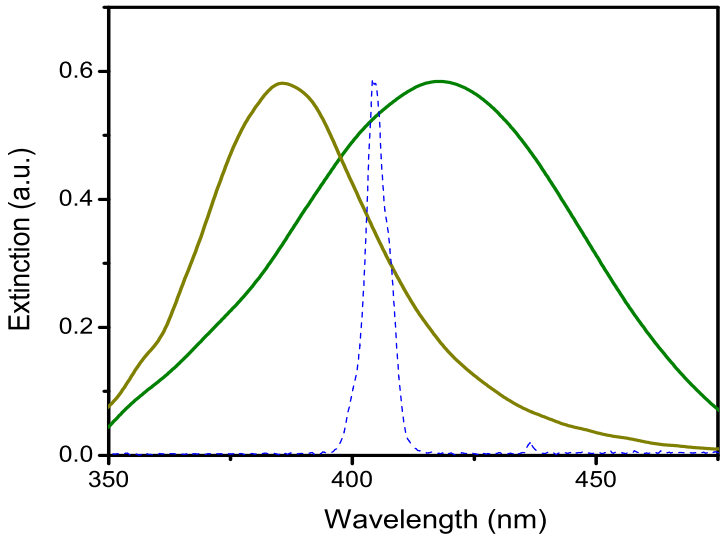

Fig. 18. Extinction spectra of aqueous solution of 25 nm (dark yellow) and 48 nm (olive) nanoparticles. The blue dashed line is an intensity spectrum of the probe beam.

The heating was continued for approximately 10 min, during which time the solution turned a turbid yellow color, as the larger particles were formed. The solution was stored at temperature close to 0^{o}C and was stable for several weeks.

The obtained colloidal solutions exhibited distinct colors, yellow for the smaller particles and yellow to greenish for the larger particles. The extinction spectra of the small and large nanoparticle samples are presented in Fig. 18. They were measured using a broad incoherent light source (halogen lamp) and a spectrometer (Ocean Optics, 2000). The resonance peaks due to the surface plasmon resonance can be clearly seen. The blue dashed line in Fig. 18 is spectrum of the probe beam.

The scanning electron microscopy (SEM) images of the samples and their size distributions are presented in Appendix A (Fig. 45). To obtain the size distribution the images were first processed in Adobe Photoshop and after that analyzed with

Scion Image software [38]. The obtained size distribution was fitted with a Gaussian function

$$\frac{1}{\sigma\sqrt{2\pi}}e^{-\frac{(d-dc)^2}{2\sigma^2}}. \tag{3.19}$$

For the smaller particles the mean diameter was found to be d_m=27 $\pm$ 1 nm with a dispersion of σ=14$\pm$1 nm, for the large particles the mean diameter is d_m=48$\pm$1 nm with a dispersion of σ=21$\pm$2 nm.

2. Experimental results and discussion

The transient response of aqueous solution of spherical silver particles of diameters 27 nm and 48 nm was studied with a femtosecond pump-probe technique. The smaller size particles were studied using the output of the oscillator, the larger size particles were studied with the amplified pulses. The energy of the pump pulses was about 2 nJ for the small particles and was set to about 10μJ for the large particles. The energy of the probe pulses was about 0.1 nJ and about 100 nJ for the small and the large diameter particles respectively. The experimental signals are presented in Fig 19. The initial peak, which is due to the fast response of the excited electron system, is followed by a damped oscillation. In the inset the oscillating part of the signals and the fit with a damped cosine function $f(t) = A\exp(-t/\tau)\cos(\omega t + \varphi)$ are shown. The obtained period of the oscillation T and the damping time τ are T=7$\pm$0.5 ps, τ=9$\pm$2 ps and T=16$\pm$1 ps, τ=18$\pm$4 ps for the samples of the small and large particles respectively. The period of the acoustic oscillations versus the diameter of the nanoparticles is presented in Fig. 20.

A near infrared pump laser pulse excites electrons in the conduction band and creates a non-thermal distribution. The energy acquired by the electron system is quickly redistributed among the electrons via electron-electron scattering. For near-

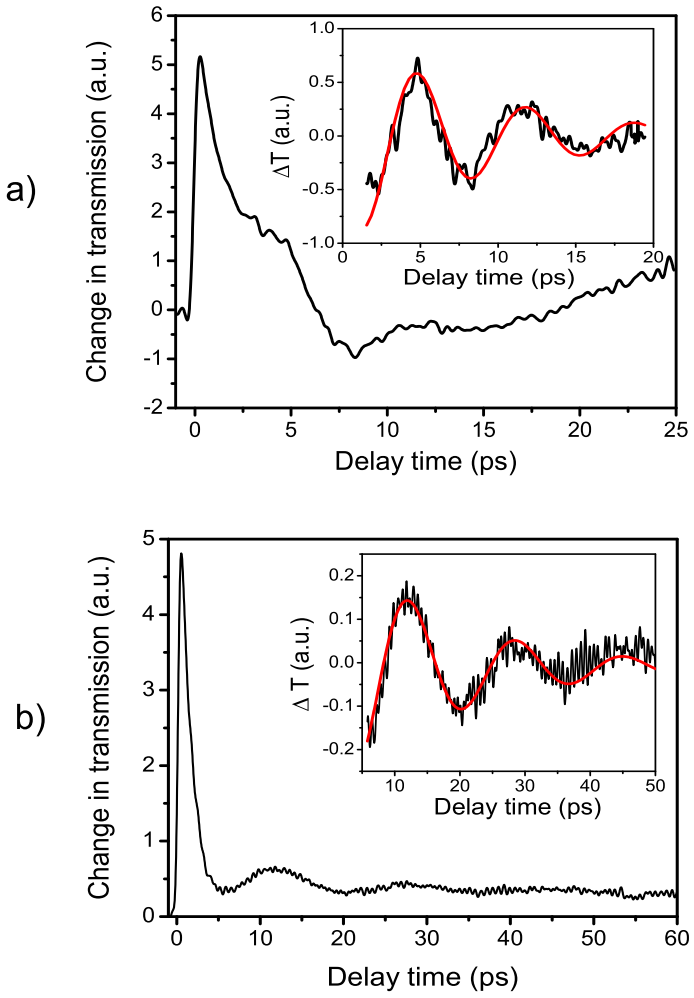

Fig. 19. Transient transmission signals from the small a) and large b) nanoparticles. The initial peak, which is due to the response of the excited electron plasma, is followed by an oscillation induced by the fundamental breathing mode. The insets show the oscillating part of the signals fitted with damped cosine functions. The obtained period of the oscillation T and the damping time τ are T=7 ps, τ=9 ps and T=16 ps, τ=18 ps for the samples of the small and large particles respectively.

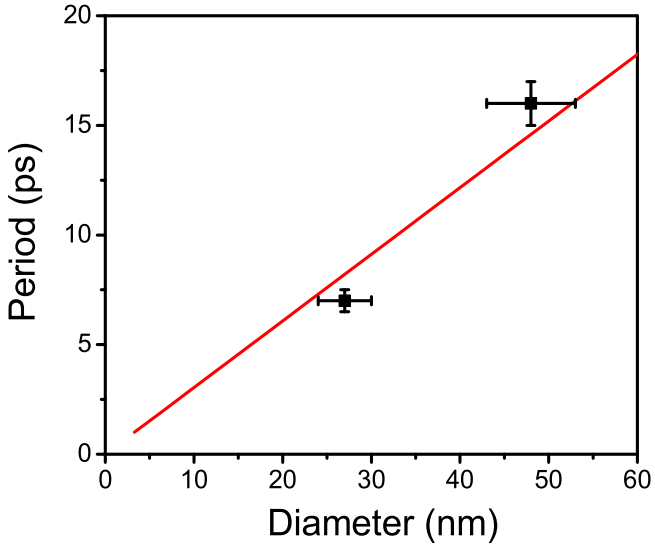

Fig. 20. Diameter of the particles versus period of the oscillations. The solid line was calculated for a sphere with elastic bulk constants for silver using Eq. 3.14.

infrared pump photons of energy $\hbar\omega \approx 1.45eV$ the thermalization time of electrons in silver nanoparticles of not very small diameter (d $\geq$ 10nm) is about 350 fs [39]. On the other hand, the excited electron system thermalizes with the lattice via electron-phonon interaction on a picosecond time scale, which is longer than the thermalization time of the excited electron gas. Neglecting the initial time, when the excited electrons have not yet acquired a thermal distribution, the dynamics of the energy transfer from the electron system to the lattice can be described in the frame of the two-temperature model. In this model the electrons and phonons are considered as two sub-systems with their own temperatures. The dynamics of this system can be described by two coupled equations

$$C_e(T_e)\frac{dT_e}{dt} = -g(T_e - T_l) \tag{3.20}$$

$$C_l\frac{dT_l}{dt} = g(T_e - T_l) - \eta(T_l - T_{media}),$$

where $C_e(T_e)$ and C_l are the electron and lattice thermal capacities, T_e and T_l are the electron and lattice temperatures, g is a constant which describes electron-phonon coupling, and T_{media} is the temperature of the surrounding medium. Note that the thermal capacity of the electron sub-system is not constant and depends on the electron temperature. Since the thermal capacity of lattice is about two orders of magnitude larger than the thermal capacity of electron, the initial electron temperature can reach very high values (on the order of a thousand ^{o}C). The transient optical response of the electron sub-system to excitation by a femtosecond laser pulse was calculated in the previous works [37] using the model of Rosei *et. al.* In this model the interband contribution of the dielectric function depends on the electron temperature (Eq. 3.4). The calculations show that the rise of the electron temperature leads to a redshift and broadening of the plasmon resonance band. This results in a decrease in the absorption at the resonance maximum (bleaching) and an increase in the absorption at the shoulders of the resonance band. The response observed in the experiment depends on the spectral position of the probe beam relative to the surface plasmon resonance peak. For the smaller size particles, the pump pulse induces an increase in the transmission of the probe beam (bleaching). For the larger particles, the response corresponds to an increase in the absorption and scattering of the probe beam.

The pump laser pulse excites electrons in the conduction band. The energy deposited into the electron system flows to the phonon modes on a picosecond time scale. If the size of the particle is larger than several nanometers, the period of the fundamental vibrational mode will be longer than the time of the heating of the lattice and impulsive excitation of this mode will occur.

The position of the maximum of the plasmon resonance depends on the electron density $\omega_p \propto \sqrt{n}$ [40]. The coherent acoustic vibrations of the particle modulate the electron density and cause a periodic change of the position of the plasmon resonance

band. This oscillation is detected by the probe beam tuned to the side of the resonance peak. For the smaller particles the oscillations are superimposed on the transient bleach signal induced by the excited electron system. For this sample the probe beam is located on the red side of the plasmon band and the initial contribution to the signal due to the expansion of the particle results in additional absorption. For the larger particles the probe beam is on the blue side of the resonance peak and the initial expansion of the particles decreases the absorption.

The period of the acoustic vibration of the particles and the average particle diameter agree with Eq. 3.14 in which the bulk elastic constants are used within the accuracy of the measurements. This result is in agreement with the previous measurements of Au nanospheres of sizes 8-120 nm and Ag nanospheres of sizes 6-30 nm, where it was found that a homogeneous elastic sphere with bulk elastic constants describes well acoustic properties of the particles with size exceeding a few nm.

Damping of the acoustic vibrations of a spherical particle due to transfer of acoustic energy from the oscillating sphere to the surrounding medium is proportional to the imaginary part of the normalized frequency (Eq. 3.15). For silver spheres in water the decay time $\tau \approx 20R/V_L^{(s)}$, which gives τ_{27nm} ≈77 ps and τ_{27nm} ≈136 ps for the smaller and larger particles respectively. The oscillations observed in the experiment decay much faster. As was suggested in the previous work [41], this can be explained by taking into account the finite size distribution of the sample. The frequency of the acoustic vibrations is inversely proportional to the size of the particle (Eq. 3.14). Particles of different sizes contribute to the observed experimental signal, which results in inhomogeneous damping of the observed signal. When the size distribution is not very broad and has Gaussian form the resulting signal can be

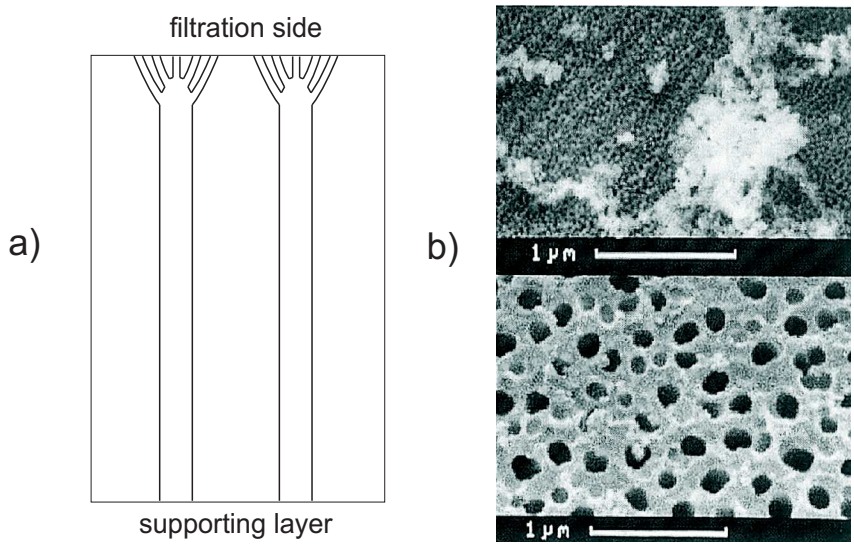

Fig. 21. Schematic representation of the cross-section of an Anodisc membrane a), and SEM micrographs of the filtration surface (top) and the supporting layer surface (bottom) b).

described by the formula

$$S(t) \sim e^{-\frac{t^2}{\tau^2}} cos(\frac{2\pi t}{T_m} + \varphi), \tag{3.21}$$

where $\tau = R_m T_m/(\sqrt{2}\pi\sigma_R)$ describes the inhomogeneous damping. Here T_m is the period corresponding to the mean radius of the particles R_m.

D. Coherent Acoustic Vibrations in Silver and Bismuth Nanowires

1. Samples preparation

Silver and bismuth nanowires of high aspect ratio were produced by the template-assisted potentiostatic electrodeposition method [24]. Commercially available filter membranes were used as the templates.

For growth of Ag nanowires of the larger size ("large size") porous anodic aluminum oxide membranes (Whatman Company, Anodisk) with the nominal pore diameter of 20 nm were used. The structure of these membranes is illustrated in Fig. 21

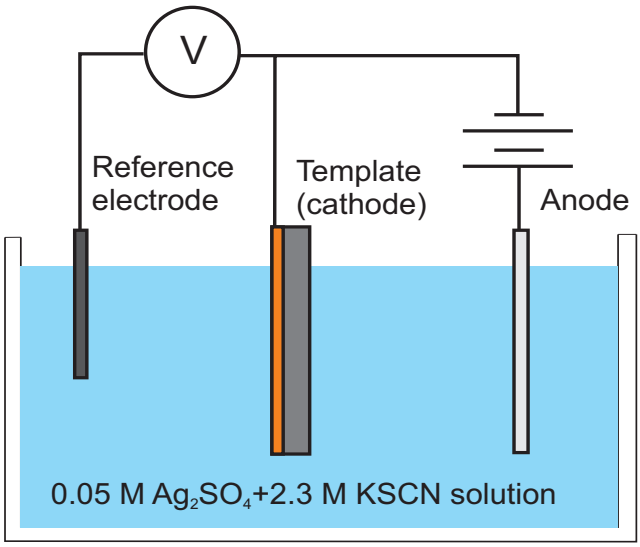

Fig. 22. Schematic diagram of the experimental setup for potentiostatic electrodeposition growth of silver nanowires in a porous anodic aluminum oxide membrane.

[42]. The main part of the membrane consists of a layer of thickness of about 55 μm forming large pores of diameter of 150-200 nm (support layer). On one side of the membrane these large pores branch and become smaller in diameter. This side of the membrane is used for filtration (filtration side). The diameter of the pores at the filtration surface is about 20 nm, corresponding to the pore size claimed by the company. The aluminum oxide membranes have high porosity ($\sim$ 0.5 at the filtration surface and $\sim$ 0.3 at the reverse side surface) and the pores in these membranes are arranged in a hexagonal array. To establish an electrical contact, a gold film of thickness of about 100 nm was deposited by a thermal evaporation method on the filtration side of the membrane. The other side of the membrane (the support layer) was used as a template for the nanowires growth. The electrodeposition was performed at room temperature in 0.05 M Ag_2SO_4+2.3 M KSCN solution, pH=6.0-6.5 (Fig. 22). The anode was a platinum plate of the size of 20 mm by 50 mm. The separation distance between the membrane and the anode was set to about 30 mm.

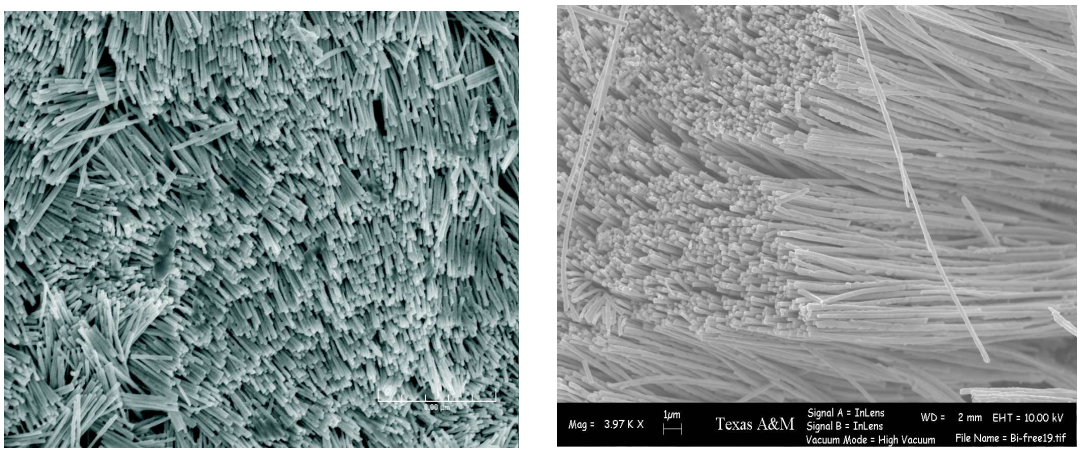

a) b)

Fig. 23. SEM micrographs of Ag a) and Bi b) nanowires standing on a glass substrate.

An Ag/AgCl (3 M NaCl) electrode was used as a reference with respect to which all potentials were measured. The overpotential voltage at the cathode η, defined as $\eta = E(I) - E_0$, where $E(I)$ and E_0 are the applied and equilibrium potentials of the electrode, was set to -0.25 V. After filling the pores with nanowires the membrane was polished from both sides with Al_2O_3 powder in order to remove the gold film and the excess of silver deposited on the surface. Next, the membrane was glued to a glass slide and the aluminum oxide template was removed by dissolving in a 5 wt% NaOH solution at room temperature for 1 hour, leaving free standing nanowires on a glass slide (Fig. 23). For TEM analysis the nanowires were shacked off in a sonicating bath. The preparation method of bismuth nanowires of the diameter 200 nm is similar to the above procedure.

Silver and bismuth nanowires of smaller diameter ("small size") were produced using a polycarbonate membranes (SPI, SPI-pore) of thickness of about 5 μm. The porosity of these membranes (~ 0.1) is lower than that of the aluminum oxide membranes. The pores are randomly distributed across the membrane surface, and the

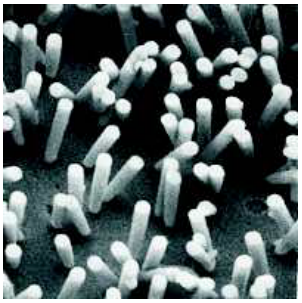

Fig. 24. An SEM image of a "corrosion cast" of a SPI-Pore membrane filter. The cast was made of the membrane filter, the membrane dissolved out, leaving the "cast" intact.

average distance between the pores is about 0.4 μm. In Fig. 24 an SEM image of a "corrosion cast" of a SPI-Pore membrane filter is shown (courtesy of www.spi.com). The procedure growing the nanowires is similar to that for the 200 nm nanowires. After filling the pores with nanowires the gold film and the excess of silver (or bismuth) deposited on the surface was removed by a cotton swab wetted in alcohol. The transient transmission measurements were performed with the samples of nanowires inside the polycarbonate membranes. Schematic representations of the large diameter and the small diameter samples used in the experiments are shown in Fig. 25.

2. Sample characterization

To obtain the size distribution of the nanowires SEM micrographs and transmission electron microscopy (TEM) micrographs of the samples were taken. To analyze the crystal structure of the material the Selective Area Electron Diffraction (SAED) images were registered at several points along the nanowire length.

The SEM images of a sample of the large silver nanowires standing on a glass slide and the size distribution obtained from five SEM images are presented in Fig. 46

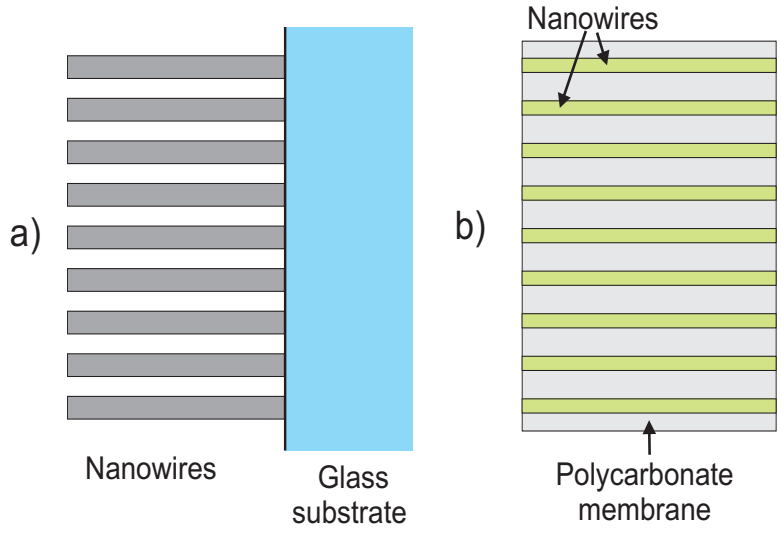

Fig. 25. Schematic representations of the cross-section of the large diameter a) and small diameter b) nanowires samples.

a) and b). The nanowires have a relatively narrow size distribution with the average diameter d = 200±1 nm and a dispersion σ=20±1 nm. The SAED images obtained at three different points along a selected nanowire are presented in Fig. 46 c). The diffraction pattern changes as we go along the wire. This suggests that a single nanowire consists of large crystallites of about a micrometer in length.

To obtain the size distribution of the small Ag nanowires first the polycarbonate matrix was dissolved and the nanowires were separated from the solution in a centrifuge machine. Then they were washed and dissolved in deionized water and a small part of the solution was deposited on a coper grid for TEM imaging. An example of the TEM image and the size distribution acquired from six TEM images and fitted with a Gaussian function are presented in Fig. 47 a) and b). The measured average diameter was d = 63±1 nm and a dispersion σ=8±1 nm. The SAED images obtained at two different points of one of the nanowires are presented in Fig. 47 c). Similar to the larger nanowires the diffraction images are different at these two points.

One of the TEM images taken from the large Bi nanowires and the size distribu-

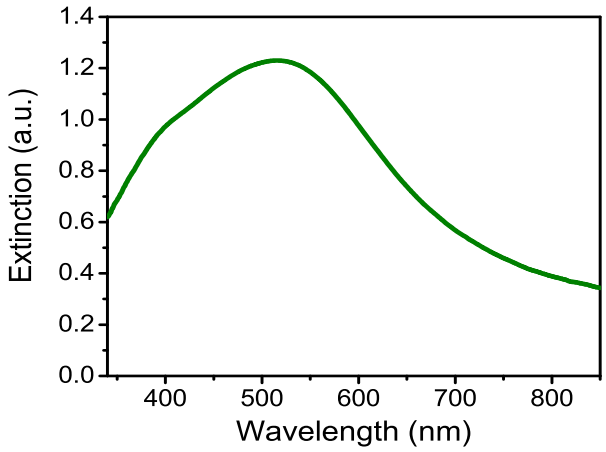

Fig. 26. Extinction spectrum of a sample of Ag nanowires of small diameter inside a polycarbonate membrane.

tion acquired from two TEM micrographs are presented in Fig. 48 a) and b). The size distribution of the sample obtained from the TEM images appears to be worse than for the other three samples. There appear two peaks sitting on a pedestal. The large peak is centered at 196 nm and the smaller and narrower peak at 240 nm. The SAED images obtained at three different points along one selected nanowire are presented in Fig. 48 c).

A TEM image of the small Bi nanowires and the size distribution acquired from six TEM images are presented in Fig. 49 a) and b). The average diameter obtained from the fit is D = 74±1 nm and a dispersion σ=8±1 nm. The SAED images obtained at two different points of one of the nanowires are presented in Fig. 49 c).

The extinction spectrum of a sample of the small diameter Ag nanowires inside a polycarbonate membrane is presented in Fig. 26. The measurement was done similarly to the spectral measurements of the solution of Ag nanospheres described in the previous part of this chapter. The light was incident perpendicular to the surface of the membrane. The broad resonance peak with the maximum around 530 nm can

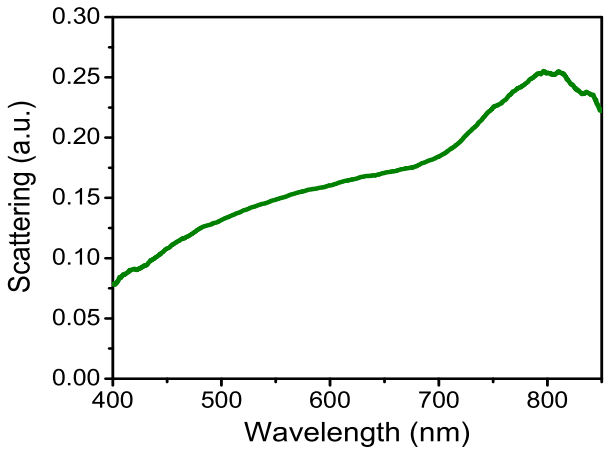

Fig. 27. The normalized spectrum of the light scattered from the surface of the large diameter Ag nanowires sample.

be attributed to the surface plasmon resonance in the nanowires. The sample has a green color. The transmission through the sample is about 10 % at 400 nm and about 50 % at 800 nm.

For the larger nanowires standing on a substrate the density of the nanowires is much higher and almost all light incident on the surface of the sample is absorbed or scattered. The sample has a mute white color, with the metallic shine similar to the bulk silver. The optical properties of this sample were characterized by a spectrum of the light scattered from the surface of the sample (Fig. 27). It should be noted that the equation 3.9 cannot be readily applied to this sample. First, the diameter of these wires becomes comparable to the wavelength of the incident light so that the retardation effects need to be taken into account. Also at these densities, when the distance between the nanowires is about the wavelength of the incident light, the interaction between the nanowires cannot be neglected [30].

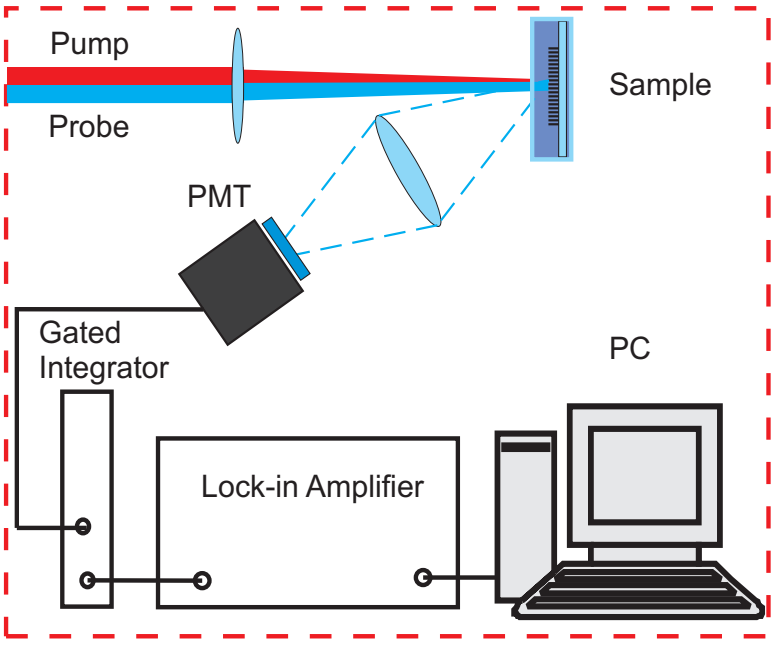

Fig. 28. Experimental arrangement for the scattering experiments with nanowires.

3. Scattering configuration

In the experiments with nanowires, the detection part of the transient transmission setup was modified (Fig. 28). The infrared pump and the blue probe beams were focused into a spot of about 0.6 mm and 0.4 mm diameter respectively. The probe light scattered from the surface of the sample was collected with a lens with a focal length f=10 cm and a diameter d=10 cm. The collected light was directed into a cooled photomultiplied tube (EMI 6255B). A blue filter (Schott, BG 12) was placed in front of the PMT to block the scattered pump light. The output of the PMT was terminated with a 50 Ω resistor and connected to the input of a gated integrator (SRS, SR 250). The gated integrator was set to the "last sample" mode (no averaging). The output of the integrator was connected to a lock-in amplifier (Princeton Applied Research System, PARS), with an integration time set to 1 s. The output of the amplifier was connected to a PC with a data acquisition card and the data was stored

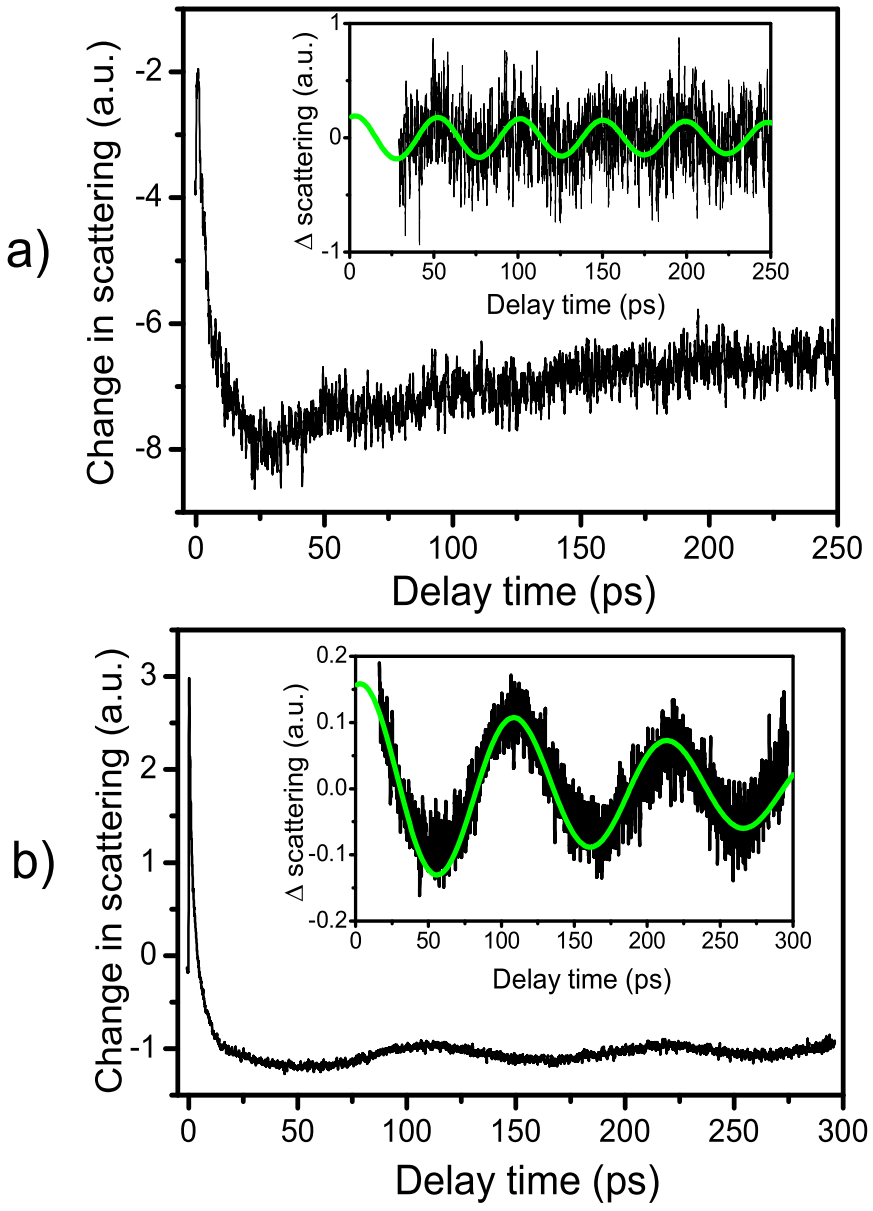

Fig. 29. Transient signals measured from the small size Bi nanowires a) and the large size Bi nanowires b). The insets show the oscillating parts of the signals fitted with a damped cosine function (see the text). The obtained oscillation periods T and the damping times τ are T=49 ps, τ=700 ps for the small size nanowires and T=105 ps, τ=450 ps for the large size nanowires respectively.

in the computer.

4. Acoustic vibrations in Bi nanowires

Bi nanowires of the small size in a polycarbonate membrane and of the large size standing on a glass substrate were studied. The energy of the pump pulses was set to 1μJ for the smaller diameter sample and to 2μJ for the larger diameter sample. The energy of the probe pulses was 100 nJ. The measured signals are presented in Fig. 29. For the smaller diameter nanowires sample the signal-to-noise ration is worse compared to that of the larger diameter nanowire sample. The initial peak, which is due to the transient response of the excited carriers, is followed by an oscillating signal. The oscillation was fitted with a damped cosine function $exp(-\frac{t}{\tau})cos(\omega t+\phi)$. The obtained oscillation periods T and the damping times τ are T=49 ps, τ=700 ps for the small size nanowires and T=105 ps, τ=450 ps for the large size nanowires respectively.

5. Acoustic vibrations of Ag nanowires (low excitation)

The small size Ag nanowires in a polycarbonate membrane and the large size nanowires standing on a glass substrate were studied. The energy of the pump pulses was about 1 μJ for the small size nanowires and 2 μJ for the large size nanowires. The energy of the probe pulses was 100 nJ. The measured signals are presented in Fig. 30. Similar to the experimental signals of the Ag nanospheres, the initial response of the excited electron system is followed by an oscillating signal. The oscillating part of the signal was fitted with a damped cosine function $exp(-\frac{t}{\tau})cos(\omega t+\phi)$. The obtained oscillation periods T and the damping times τ are T=28.4 ps, τ=150 ps for the small size nanowires and T=71 ps, τ=200 ps for the large size nanowires respectively.

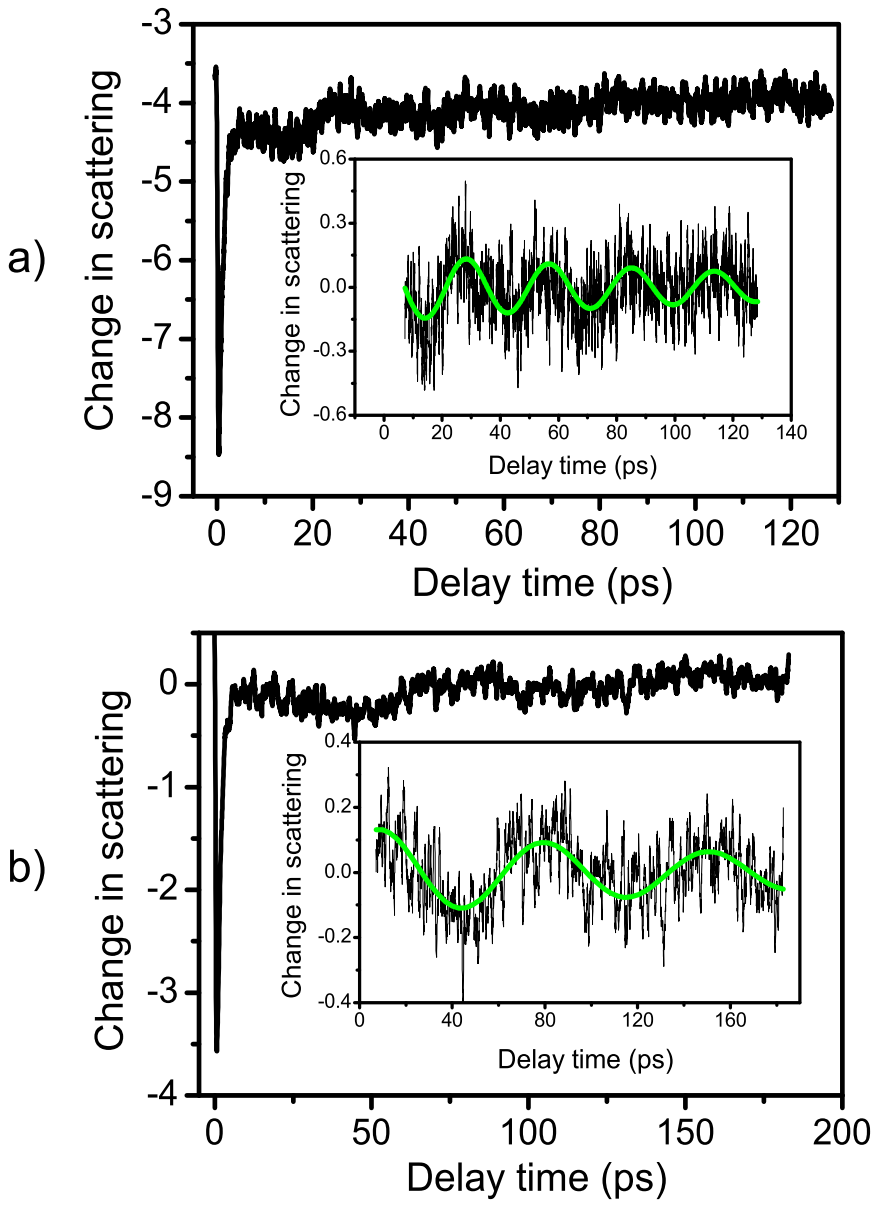

Fig. 30. Transient signal measured from the small size Ag nanowires a) and the large size Ag nanowires b). The insets show the oscillating parts of the signals fitted with a damped cosine function (see the text). The obtained oscillation periods T and the damping times τ are T=28.4 ps, τ=150 ps for the small size nanowires and T=71 ps, τ=200 ps for the large size nanowires respectively.

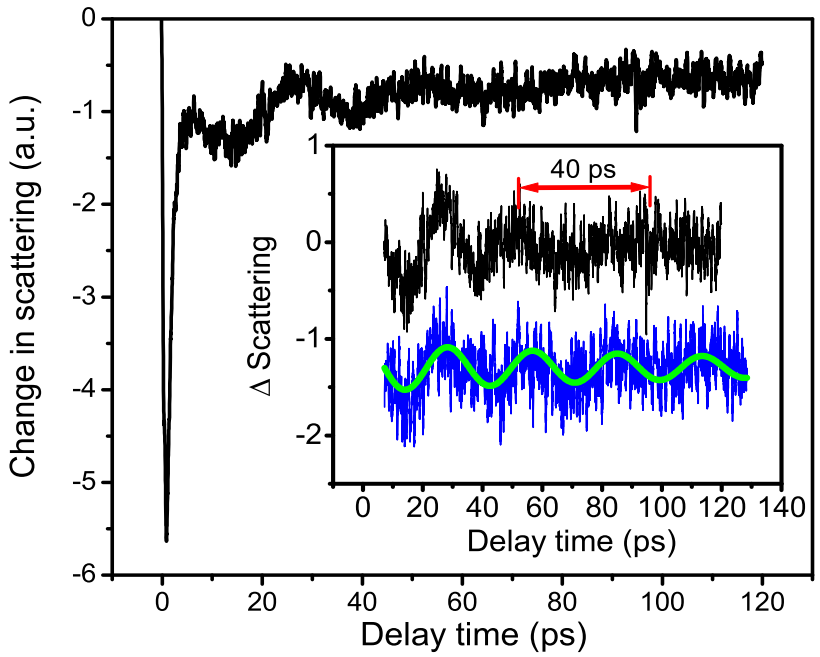

Fig. 31. Transient signal measured from the small size Ag nanowires. The energy of the pump pulses was about 2μJ. The inset shows the oscillating part of this signal and the oscillation from the low excitation measurements.

6. Acoustic oscillations of Ag nanowires (high excitation)

The experimental signals measured with the small and the large size nanowires are presented in Fig. 31 and Fig. 32. For both samples the experimental signals are average over several measurements performed on the same spot of the sample. The energy of the probe pulses was 100 nJ for both samples. The energy of the pump pulses was set to 2μJ for the small nanowires and 20μJ for the large nanowires. The inset shows the oscillating part of the signal (black). Also the acoustic signal obtained from the same sample with the low energy pump pulses and the fit are shown for reference (blue and green).

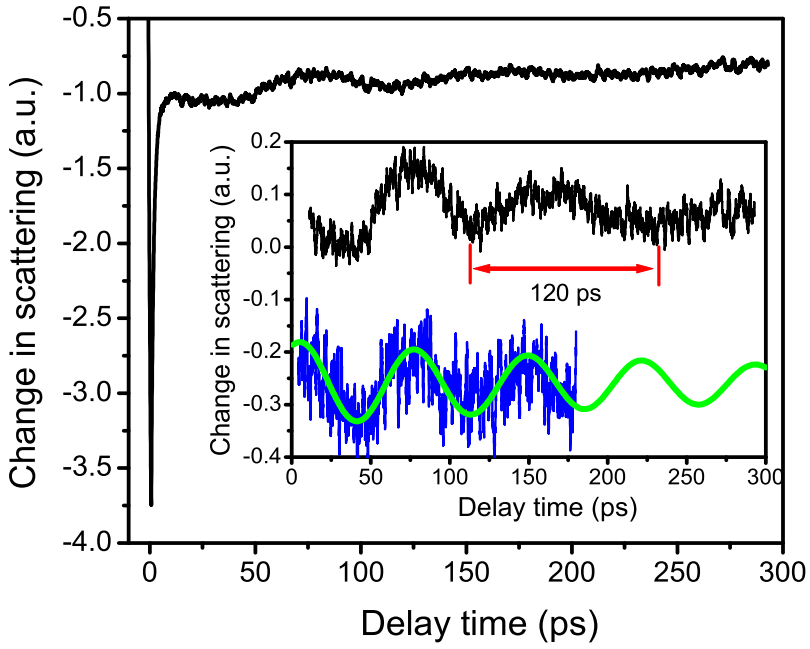

Fig. 32. Transient signal measured from the large size Ag nanowires. The energy of the pump pulses was about 20μJ. The inset shows the oscillating part of this signal and the oscillation from the low excitation measurements.

E. Discussion

The transient signals obtained from all four samples studied in the present work exhibit oscillations induced by the coherent acoustic vibrations of the nanowires. It should be noted that in the present experiment the excitation of the nanowires by the pump pulse is inhomogeneous, especially for the samples with the large diameter nanowires, where the nanowire density is high. That means that other acoustic vibrations can be excited besides the extensional and the breathing modes. For example, an acoustic wave propagating along the nanowire can be excited. On the other hand for these very long objects the acoustic motion along the wire will happen on the nanosecond time scale, so only the breathing modes can be detected in the time delay range accessible with the experimental setup.

1. Low excitation fluence

When the intensity of the pump pulses is not very high the oscillation has a simple sinusoidal form and can be fitted with a damped cosine function. From the obtained period of the acoustic mode and the diameter of the nanowires it is possible to determine the elastic properties of the material. Equation 3.17 for the fundamental breathing mode can be rewritten as

$$\frac{2\pi}{T_0} = \frac{\tau_0 c_l}{R}, \tag{3.22}$$

where c_l is the longitudinal sound velocity, and T_0 is the period of the fundamental breathing mode. Using this equation and the values of the Poisson's ratio for the bulk material (ν=0.37 for Ag, ν=0.33 for Bi) the longitudinal sound velocities for the Ag and Bi nanowires were calculated (Table. II). For the large diameter Bi nanowires sample in which the size distribution showed two peaks, a larger one located at about

Table II. The longitudinal sound velocities calculated for the Ag and Bi nanowires using the isotropic elastic model.

	Ag (small)	Ag (large)	Bi (small)	Bi (large)
c_l(m/s)	3150	4000	2200	2715

196 nm, and a smaller one at 240 nm, the sound velocity was calculated using a diameter of 196 nm. The longitudinal sound velocities for the polycrystalline form and for different crystallographical directions of a single crystal of Ag and Bi are presented in Table III [43, 44, 45] for reference.

The values of the sound velocities obtained for both Ag samples are different from the value for the polycrystalline material. Compared to the single crystal, the sound velocity calculated for the small diameter sample has a value in between the values of the velocities in $< 1, 0, 0 >$ and $< 1, 1, 0 >$ direction, whereas that calculated for the large diameter nanowires is in between the velocities in the $< 1, 1, 0 >$ and $< 1, 1, 1 >$ directions. The acoustic properties of the nanowires depend on the structure of the material. The electron diffraction analysis of the nanowire crystal structure shows that for both samples, the nanowires consist of crystallites of a relatively large size with the length on the order of a μm. For a single crystal material, the value of the longitudinal sound velocity depends on the direction of propagation of the acoustic wave. The fundamental breathing mode corresponds to expansion and contraction in

Table III. The longitudinal sound velocities for different crystallographical directions and for the polycrystalline form (pc) of Ag and Bi.

	Direction	$< 1, 0, 0 >$	$< 1, 1, 0 >$	$< 1, 1, 1 >$	$< 0, 2^{-1/2}, 2^{-1/2} >$	pc
Ag	c_l (m/s)	2689	3710	4437		3650
Bi	c_l (m/s)	2540	2571	1972	2082	2200

the radial direction so this mode will probe the crystal properties in the directions perpendicular to the nanowire length. If the preferential crystal growth direction is different for these two samples this could result in different elastic response of these samples. On one hand, it would be natural to assume that the nanowires prefer to grow along the same crystal direction. On the other hand it is known that the structure of nanorods and nanowires strongly depend on the preparation method and the preparation parameters. To explain why the elastic response of these two samples is different an analysis of the orientation of the crystallites in the nanowires is needed.

The longitudinal sound velocity obtained for the large diameter Bi nanowires is larger than the value for the polycrystalline bulk material and than the sound velocities of the single crystal material listed in the Table. III. One of the possible explanations to this result could be that these nanowires have less defects than the bulk crystal and are correspondingly stiffer. Another possible explanation is that the nanowires have a bismuth oxide layer on their surface. It is well known that Bi oxidize easily and an oxide layer of thickness of about 10 nm can be formed on the surface of a nanowire, depending on the level of the oxidation. In this case the system of Bi core - Bi_2O_3 shell needs to be considered.

For the small diameter Bi nanowires the obtained value of the sound velocity is equal to that of the bulk material. The analysis of the nanowire structure by the SAED imaging of a selected nanowire showed that, similar to the other samples, it consists of large crystallites.

2. High excitation fluence

The transient acoustic response of Ag nanowires under excitation with intense laser radiation was studied. It was found that as the pump fluence increases above some value the shape of the experimental signal changes. For the large diameter sample,

this change happens at the pump fluence of about 0.3 mJ/cm^2 (Fig. 32). At this fluence the period of the acoustic oscillation is no longer a constant: it is smaller at the earlier time and becomes larger at the longer delay times. During the first cycle the signal looks similar to that obtained at the low pump fluence measurement with a period close to 71 ps. At later times the period is on the order of 120 ps. Also the damping appears to have increased. It should be noted that these signals are averaged over several measurements performed on the same spot of the sample, so the effect of the sample degradation during the measurement can be excluded. A possible explanation to this change in the shape of the signal could be softening of the material or even a transition to the melted state of the nanowires. To estimate the period of the acoustic vibrations of the nanowire in the molten phase one could use the bulk velocity for liquid silver [46] v_l=2810 m/s. Assuming that ν=0.5, equation 3.22 gives the period of the fundamental breathing mode of a cylinder of the diameter d=200 nm to be T=93 ps. This value is somewhat smaller than the distance between the crests indicated in Fig 32. To estimate the temperature increase of the nanowires, we assumed the porosity of the nanowires to be 0.3, that all the energy of the pump pulse is absorbed in the nanowires, and that the energy is deposited in the tip of the nanowires in the layer of 20 nm thickness. Using the density and the heat capacity of bulk silver gives a temperature increase of about 500 ^{o}C, which is lower than the melting temperature of the bulk silver (962^{o}C). For the small diameter Ag sample, the change in the form of the experimental signal happens at a pump fluence of about 0.04 mJ/cm^2 (Fig. 31). An estimate of the period of the oscillation corresponding to the melted phase gives a value of 35 ps.

CHAPTER IV

COHERENT OPTICAL PHONONS IN BISMUTH

Dynamics of coherent optical phonons in Bi excited with femtosecond laser pulses have attracted attention in recent years. In this material, a short femtosecond laser pulse promotes electrons from the valence band to the conduction band and shifts the equilibrium positions of the atoms in the lattice, thereby creating the coherent lattice vibrations. At low pump fluences, the fully symmetric breathing A_{1g} Raman-active mode was observed at the frequency of 2.92 THz [47], in agreement with the conventional Raman scattering measurements [48]. In the experiments with the high levels of photoexcitation, a decrease of the frequency of the phonon mode was observed [49]. This phenomenon can be explained by the lattice softening due to the photoexcitation of the electrons [50] or by the effect of the lattice anharmonicity [49].

The dynamics of the coherent optical phonons in Bi film were studied in the present work with a femtosecond pump-probe technique. The optical phonons were excited at several pump fluences. The excitation with two pump pulses, where the first pulse prepares the state of with a certain density of photoexcited carriers, and the second pulse excites the coherent mode, was employed. Numerical simulation of the transient reflectivity response, including excitation inhomogeneity, were done.

This chapter has the following structure. The discussion of the lattice structure of Bi, a theoretical description of coherent phonons, and the excitation mechanism are presented in the first part. The second part describes the numerical model which was used to model the observed signals. In the third section the experimental results of the low excitation measurements are discussed, followed by the experimental results of the measurements taken with high intensity laser pulses.

A. Theoretical Description

1. Lattice structure

Bismuth crystallizes to A7 (arsenic) crystal structure with the $\overline{3}$m point group symmetry. The primitive cell is rhombohedral and contains two atoms (Fig 33). The A7 structure is similar to a simple-cubic structure to which two independent distortions have been applied. The first distortion is a stretching along a body diagonal. This diagonal retains its 3-fold symmetry and becomes the trigonal axis of the A7 structure. The second distortion is an internal shifting of alternate atoms toward each other along the trigonal axis. The resulting structure is composed of layers of atoms perpendicular to the trigonal axis with alternate larger and smaller spacing. The interaction of the laser radiation with the optical phonons is determined by the Raman tensors. The three Raman active modes at the center of the Brillouin zone are A_{1g} (totally symmetric breathing) and E_g (doubly degenerate). The Raman tensors of these modes are presented in Table IV.

Table IV. Raman tensors of bismuth.

a	0	0	c	0	0	0	-c	-d
0	a	0	0	-c	d	-c	0	0
0	0	b	0	d	0	-d	0	0
	A_{1g}			E_g			E_g	

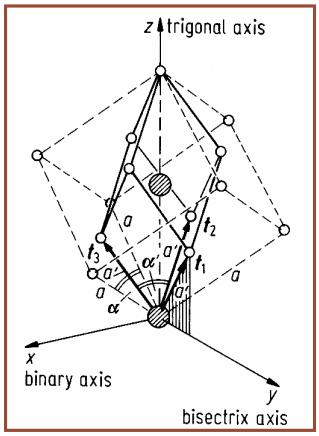

Fig. 33. The rhombohedral structure of Bi: a cubic lattice with slight displacement of the atoms. The unit cell consists of two basis atoms (hatched circles); each small circle represents another basis pair of such two atoms. For Bi $\alpha = 57^o16'$ as opposed to the value $\alpha = 60^o$ for face centered cube.

2. Theoretical description of coherent lattice vibrations

Phenomenologically, the coherent vibrational motion of atoms in a lattice can be described by a harmonic oscillator model

$$\frac{d^2Q}{dt^2} + 2\gamma\frac{dQ}{dt} + \omega_0^2 Q = \frac{1}{m}f(t), \tag{4.1}$$

where Q is the phonon mode amplitude, ω_0 is the frequency, γ is the decay rate, and $f(t)$ is the force that drives the phonon mode. If the displacement and the velocity at the initial moment of time are equal to zero the solution of this equation has the form [51]

$$Q(t) = \int_{-\infty}^{t} \frac{F(\tau)e^{-\gamma(t-\tau)}sin(\sqrt{\omega_0^2 - \gamma^2}(t-\tau))}{m\sqrt{\omega_0^2 - \gamma^2}}. \tag{4.2}$$

For an impulsive force, which has the delta function time dependence

$$F(t) = I_0\delta(t) \tag{4.3}$$

the solution for the lattice displacement is

$$Q(t) = \frac{I_0}{m\sqrt{\omega_0^2 - \gamma^2}}\theta(t)e^{-\gamma t}sin(\sqrt{\omega_0^2 - \gamma^2}t). \tag{4.4}$$

Here $\theta(t)$ is a step function. An example of this type of process is stimulated Raman scattering in transparent media. The laser pulse provides a momentum to the phonon mode ("kicks") and the nuclei start to oscillate around their equilibrium position. For a displacive force

$$F(t) = D_0\theta(t) \tag{4.5}$$

the solution is

$$Q(t) = \frac{D_0}{m\omega_0^2}\theta(t)\left(1 - e^{-\gamma t}\left[(cos(\sqrt{\omega_0^2 - \gamma^2}t) + \frac{\gamma}{\sqrt{\omega_0^2 - \gamma^2}}sin(\sqrt{\omega_0^2 - \gamma^2}t)\right]\right). \tag{4.6}$$

An example of the displacive excitation process is excitation of coherent phonons in absorbing media. The excitation force shifts the equilibrium lattice position and the nuclei start to oscillate around this new equilibrium.

The harmonic oscillator model provides a simple phenomenological description, leaving open a question about the definition of the amplitude of the coherent phonon mode. The quantum mechanical description was developed by Kuznetsov *et al.* [52] to provide answers to this questions. Consider a simplified model of a two-band semiconductor with the Hamiltonian

$$H = \sum_{\mathbf{k},\alpha}\varepsilon_{\alpha\mathbf{k}}c^\dagger_{\alpha\mathbf{k}}c_{\alpha\mathbf{k}} + \sum_{\mathbf{q}}\hbar\omega_{\mathbf{q}}b^\dagger_{\mathbf{q}}b_{\mathbf{q}} + \sum_{\alpha,\mathbf{k},\mathbf{q}}M_{\mathbf{k},\mathbf{q}}(b_{\mathbf{q}} + b^\dagger_{-\mathbf{q}})c^\dagger_{\alpha\mathbf{k}}c_{\alpha\mathbf{k}+\mathbf{q}}, \tag{4.7}$$

where $c_{\alpha\mathbf{k}}$ and $c^\dagger_{\alpha\mathbf{k}}$ are the creation and annihilation electron operators, $\varepsilon_{\alpha\mathbf{k}}$ describes

the energy band (conduction or valence); $b^{\dagger}_{\mathbf{q}}$ and $b_{\mathbf{q}}$ are the creation and annihilation operators of the phonons, $\omega_{\mathbf{q}}$ is the phonon frequency; $M_{\mathbf{k},\mathbf{q}}$ describes the deformation coupling. The first term in the Hamiltonian describes the electrons and holes in the static crystal, the second term corresponds to the phonons, and the last term describes electron-phonon interaction (deformation coupling). The phonon operators are related to the lattice displacement operator $\hat{u}$

$$\hat{u} = \sum_{\mathbf{q}} \sqrt{\frac{\hbar}{2\rho V \omega_{\mathbf{q}}}} (b_{\mathbf{q}} e^{i\mathbf{qr}} + b^{\dagger}_{\mathbf{q}} e^{-i\mathbf{qr}}), \tag{4.8}$$

where ρ is the reduced mass density and V is the volume of the system. The coherent amplitude of the $\mathbf{q}$th mode is defined as

$$D_{\mathbf{q}} \equiv < b_{\mathbf{q}} > + < b^{\dagger}_{-\mathbf{q}} > \equiv B_{\mathbf{q}} + B^{*}_{-\mathbf{q}}, \tag{4.9}$$

so it is proportional to the Fourier components of the displacement

$$< \hat{u}_{\mathbf{q}} > \equiv < \frac{1}{V} \int d^3\mathbf{r} \hat{u}(\mathbf{r}) e^{-i\mathbf{qr}} > = \sqrt{\frac{\hbar}{2\rho V \omega_{\mathbf{q}}}} D_{\mathbf{q}} \tag{4.10}$$

If the phonon oscillator is in one of its eigenstates the average displacement of the lattice is zero, though there are fluctuations with the mean square of the displacement proportional to the number of the phonons in the mode. These are the incoherent phonons. However, in the coherent superposition of different eigenstates the displacement in general will not average to zero. An extreme case of such superposition states are coherent states

$$\Psi^{coh} = |z> = \sum_{n} \frac{z^n}{\sqrt{n!}} e^{-z^2/2} |n> \tag{4.11}$$

These "fully coherent" states involve contributions of states with an arbitrary large number of phonons. In these states

$$N^{coh}_{\mathbf{q}} = < z | b^{\dagger}_{\mathbf{q}} b_{\mathbf{q}} | z > = |z|^2 = |B_{\mathbf{q}}|^2 \tag{4.12}$$

In a general case a mode can have a certain number of both coherent and incoherent phonons

$$N_{\mathbf{q}} == |B_{\mathbf{q}}|^2 + (< |b^{\dagger}_{\mathbf{q}} b_{\mathbf{q}}| > - < |b^{\dagger}_{\mathbf{q}}| >< |b_{\mathbf{q}}| >) = N^{coh}_{\mathbf{q}} + N^{incoh}_{\mathbf{q}} \tag{4.13}$$

The equation of motion for the coherent amplitude $D_{\mathbf{q}}$ has the form

$$\frac{\partial^2}{\partial t^2} D_{\mathbf{q}} + \omega^2_{\mathbf{q}} D_{\mathbf{q}} = -2\omega_{\mathbf{q}} \sum_{\alpha,\mathbf{k}} M^{\alpha}_{\mathbf{kq}} n^{\alpha}_{\mathbf{k},\mathbf{k+q}}. \tag{4.14}$$

Here, $n^{\alpha}_{\mathbf{k},\mathbf{k+q}} =< c^{\dagger}_{\alpha\mathbf{k}} c_{\alpha\mathbf{k+q}} >$ is the electronic density matrix. The electron-phonon interaction couples the coherent phonon amplitude to the Fourier components of the electron density with the same wave vector. This equation resembles the phenomenological equation for the harmonic oscillator, however there is no dampening term. The right-hand side implicitly depends on the optical excitation condition, since $n^{\alpha}_{\mathbf{k},\mathbf{k+q}}$ are driven by the laser field.

3. Excitation mechanism

In recent years metal and semiconductor materials have been studied with the femtosecond pump-probe technique. In a number of the materials oscillations in the reflectivity at the frequencies corresponding to the optical phonon modes of the samples have been observed. To explain these oscillations several mechanisms of excitation of coherent phonons by ultrashort laser pulses have been proposed. The two main mechanisms are the displacive excitation of coherent phonons (DECP) proposed by H.J. Zeiger *et al.* [53] and the impulsive stimulated Raman scattering (ISRS) extended to opaque systems.

In the first pump-probe experiments with Sb, Bi, Te and Ti_2O_3 only Raman-active modes of A1 symmetry were observed, although Raman active modes of other symmetry were detected in the conventional Raman measurements with the intensities

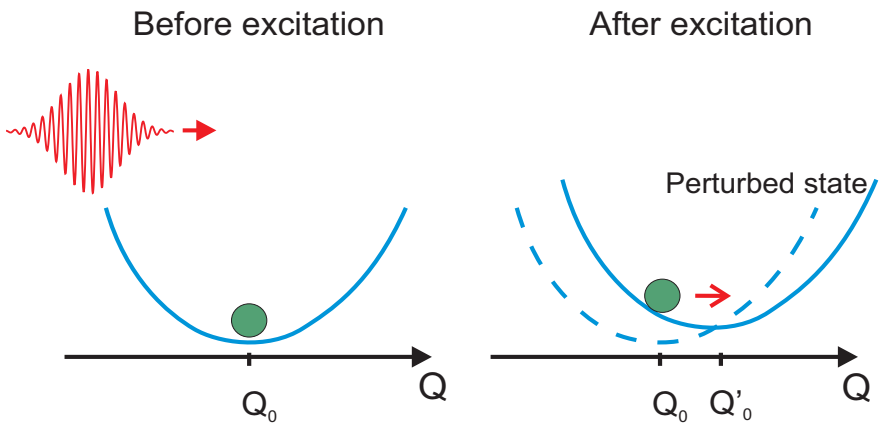

Fig. 34. Schematic diagram of excitation of coherent optical phonons by a femtosecond laser pulse.

comparable to that of the A1 mode. To explain this peculiarity as a mechanism for excitation of coherent optical phonons in this class of materials the DECP mechanism was proposed. In this model, a short laser pulse excites electrons from the valence to the conduction band which changes the occupation number of the electrons and consequently leads to a change of the equilibrium position of the atoms in the lattice. The magnitude of this shift depends on the excited carrier density. The excitation and internal thermalization of the electronic sub-system, and correspondingly change of the equilibrium position of the atoms, happens on the time scale much shorter than the response time of the lattice. On the other hand the thermalization of the excited carriers with the lattice happens on a time scale much longer than the period of the phonon mode, so the force which drives the phonon mode can be approximated as a step function. This corresponds to the temporal response of the lattice $< Q(t) > \propto 1 - cos(\omega t)$.

As these materials have been studied further the Raman active modes of symmetry other then A_1, though of smaller amplitude compared to the fully symmetric mode, were observed in the pump-probe experiments. The ISRS theory, which originally was applied to transparent material, was extended to opaque systems [17, 54]. The interaction of light with a two electron level system was considered. It was found that in general the force which drives the phonon mode has two parts. For the non-resonant Raman scattering process, which corresponds to transparent materials, the driving force has a delta function form which corresponds to the impulsive excitation with the temporal lattice response $< Q(t) > \propto sin(\omega t)$. For the resonant scattering, the driving force has a step like form, which corresponds to the displacive type excitation with the response of the lattice $< Q(t) > \propto 1 - cos(\omega t)$. Unlike the DECP model where only modes with $\mathbf{q}$=0 are excited, the ISRS requires the phase matching

$$\mathbf{k}_s - \mathbf{k}_i = \mathbf{q}, \tag{4.15}$$

$$\omega_s - \omega_i = \omega_{\mathbf{q}}. \tag{4.16}$$

B. Numerical Model

1. Excitation of the coherent phonons

Consider a femtosecond laser pulse incident on the surface of a Bi film (Fig. 35). Since the pump beam diameter is much larger than the absorption length of the pump and probe beams inside the sample, the diffusion of the carriers and the thermal transport in the lateral direction can be neglected for the time scale of interest and the situation can be reduced to a one dimension problem. Choose the coordinate system such that the z axis is perpendicular to the surface and is directed inside the sample and the origin is at the surface. Neglecting the pump pulse duration and assuming linear

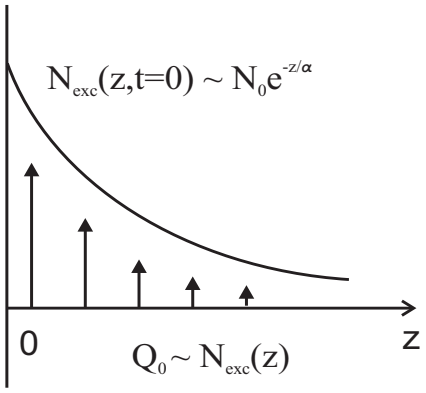

Fig. 35. Excitation of coherent phonons by a laser pulse.

absorption the density of the photoexcitated carriers inside the sample at the initial moment of time is

$$N(z, t = 0) = \alpha \frac{F_{pump}}{\hbar\omega} e^{-\alpha z}. \tag{4.17}$$

Here $N(z, t)$ is the density of the photoexcited carriers, F_{pump} is the pump fluence at the surface, and α is the linear absorption coefficient. The initial change in the equilibrium lattice position due to excitation by a pump laser pulse is proportional to the absorbed energy

$$Q_0(z) \sim N(z, t = 0) \sim e^{-\alpha z}. \tag{4.18}$$

Following the DECP model the temporal response of the lattice nuclei at the depth z to a displacive excitation can be written as

$$Q(z, t) = Q_0 e^{-\gamma t}(1 - cos(\omega t)) \tag{4.19}$$

2. Reflection from the sample

The lattice vibrations excited in the sample induce changes in the refractive index of the material via diagonal elements of the Raman tensor and can be probed through the variations induced in the optical reflectivity. The dielectric function of the material can be written as $\varepsilon = \varepsilon_0 + \delta\varepsilon_r^R + i\delta\varepsilon_i^R$. Here ε_0 is the dielectric function of the medium without the coherent vibrations of the lattice and $\delta\varepsilon_r^R$ and $\delta\varepsilon_i^R$ are the change in the real and imaginary parts of the dielectric function induced by the coherent lattice vibrations. Following T.E. Stevens *et al.* [55] the polarization induced by the lattice vibrations has the form

$$P_k^R(t) = \frac{1}{2\pi}\sum_l \int_{-\infty}^{+\infty}\int_{-\infty}^{+\infty} e^{-i(\omega-\Omega)t}\chi_{kl}^R(\omega,\omega-\Omega)E_l(\omega)Q^*(\Omega)d\omega d\Omega \tag{4.20}$$

where χ_{kl}^R is the Raman succeptibility tensor, and E_l is the electric field of the probe laser pulse. For an opaque medium, considering only the resonance contribution of the two band process, the Raman tensor can be written in terms of the linear dielectric tensor $\varepsilon_{ij}(\omega)$

$$\chi_{kl}^R(\omega,\omega+\Omega) \approx \frac{\Xi}{4\pi\hbar}\left(\frac{dRe(\varepsilon)}{d\omega} + i\frac{dIm(\varepsilon)}{d\omega}\right), \tag{4.21}$$

where Ξ describes the electron-phonon interaction. Then the changes in real and imaginary parts of the dielectric function induced by the coherent vibrations are related

$$\frac{\delta\varepsilon_r^R}{\delta\varepsilon_i^R} = \frac{dRe(\varepsilon_0)}{d\omega} \Big/ \frac{dIm(\varepsilon_0)}{d\omega}. \tag{4.22}$$

Reflection of the probe beam from the surface of the bismuth film was simulated using transfer matrix method [56]. Consider a slab a material irradiated from the left (Fig 36). The slab was divided into layers of equal thickness d. The optical properties of each layer i are characterized by a complex scalar dielectric constant ε_i.

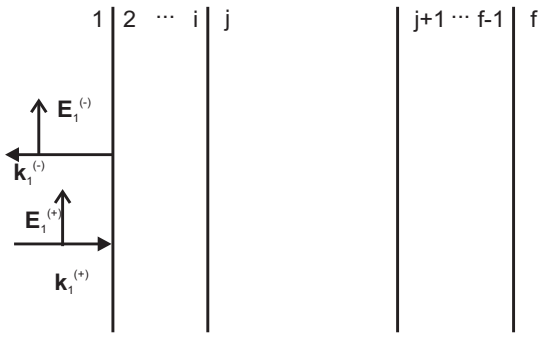

Fig. 36. Schematic of the multilayer medium.

The forward and backward propagating electric fields in layer i can be written as

$$E_i^+ = E_i^+ exp(\pm i n_i k_0 z - i\omega t) \tag{4.23}$$

Here the angle of incidence of the laser beam of 90^o was assumed. The relationship between the amplitudes of the E adjacent to the i-j interface is

$$E_i = M_{ij} E_j, \tag{4.24}$$

where M_{ij} is the transfer matrix of the i-j interface. For isotropic media the M is defined by

$$M_{ij} = \frac{1}{t_{ij}} \begin{bmatrix} 1 & r_{ij} \\ r_{ij} & 1 \end{bmatrix}, \tag{4.25}$$

where r_{ij} and t_{ij} are the reflection and transmission amplitudes for the light incident on the i-j interface from medium i. The reflection and transmission amplitudes are given by

$$r_{ij} = \frac{n_i - n_j}{n_i + n_j}, t_{ij} = \frac{2n_i}{n_i + n_j}, \tag{4.26}$$

where $n = n_r + i n_i$ is the complex index of refraction. The propagation matrix Φ

account for the phase and amplitude changes in the fields from the left-hand side to the right-hand side of layer i:

$$\mathbf{E}_i(z_i + d) = \Phi_i \mathbf{E}_i(z_i), \tag{4.27}$$

where

$$\Phi_i = \begin{bmatrix} \phi_i & 0 \\ 0 & \overline{\phi}_i \end{bmatrix}, \tag{4.28}$$

with $\phi_i = exp(in_i k_0 d_i)$.

The overall transfer matrix has the form

$$T = M_{f(f-1)} \Phi_{f-1} ... \Phi_2 M_{21}. \tag{4.29}$$

The overall reflection amplitude r for a beam incident from the left is given by

$$r = -T_{21}/T_{22}, \tag{4.30}$$

where T_{21} and T_{22} are matrix elements of the matrix T.

C. Coherent Optical Phonons in Bismuth

1. Experimental

The experimental setup for studying coherent optical phonons in Bi film is similar to that described in Chapter II except that the optical phonons were measured in reflection geometry. This is illustrated in Fig 37. The pump beam and the probe beams were focused on the surface of the sample to spots of diameter 0.6 and 0.4 mm respectively. The probe and the reference beams reflected from the surface of the sample was detected by large-area photodiodes (UDT-PIN 10D). Blue filters (Schott BG12) was placed in front of the photodiode to block the pump beam. In the double-

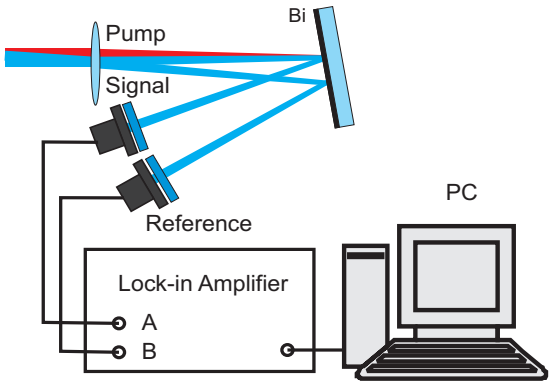

Fig. 37. Experimental arrangement for detection of the reflected light.

pulse excitation experiments the pump beam was split in two parts by a 50/50 beam splitter. The delay between the pump beams was controlled by a mechanical translation stage. The intensity of each beam was adjusted by a neutral optical density filter.

The bismuth film was deposited in vacuum onto glass slides by thermal vapor deposition method at the deposition rate 0.5 nm/s. The electron diffraction analysis showed that the film has polycrystalline structure. Information on the real and imaginary parts of the refractive index found in the literature for Bi films and crystal is presented in Fig. 38.

2. Single pump pulse excitation

The transient reflectivity signal measured at the pump fluence of 0.5 mJ/cm^2 is presented in Fig. 39. The signal consist of an oscillation induced by the coherent lattice vibrations and a transient background. The background is resulting from the response of the photoexcited electrons. The inset shows the Fourier transform of the oscillating part of the signal. The peak frequency of the Fourier spectrum f=2.93

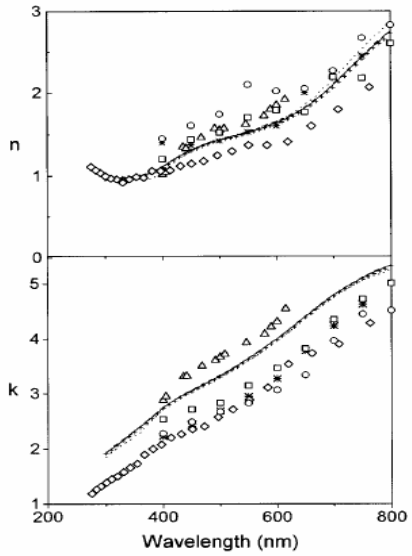

Fig. 38. Real (n) and imaginary (k) parts of the refractive index of Bi as a function of wavelength. The results were obtained in a PDL films of thicknesses (—)100 nm, (+++) 66 nm, (---) 40 nm, and (···) 20 nm [57]; in Bi film (△) [58] and (∗) [59] and for bulk crystalline Bi (⋄)in ref [60] and (⊓) basal plane and (◯) optic axis in ref [61].

THz is in agreement with the A_{1g} phonon mode obtained from the Raman scattering measurements in Bi [48]. The decay time of the oscillations is about 7 ps.

3. Optical control of coherent lattice vibrations

It is possible to control the coherent motion of nuclei in the lattice by applying a sequence of optical pulses with specially selected amplitudes and relative delays. The simplest example would be to use only two pump pulses. In the experiment, the fluence of the first pump beam was set to about 3 mJ/cm^2, the energy of the second pump pulse was set to a somewhat smaller value (about 2.8 mJ/cm^2). The results are presented in Fig. 40. In part a) the transient response to a single pulse excitation is shown. Fig. 40 b) shows the result when the second pulse is delayed with respect

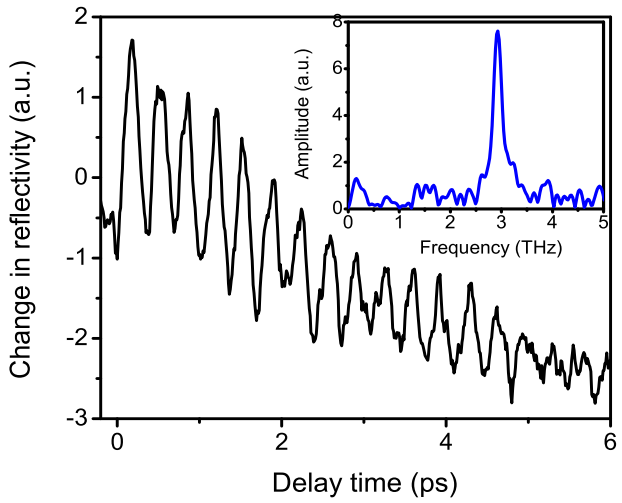

Fig. 39. Transient reflectivity signal obtained at 0.5 mJ/cm^2 pump fluence.

to the first pump pulse by one period of the oscillation. Clearly the amplitude of the lattice vibration increase. When the second pump is delayed by about a half of the period, these oscillations vanish.

D. High Pump Fluences Measurements

1. Excitation with one pump pulse

Experimental results for excitation at different pump fluences are presented in Fig. 41. In part a) the time domain traces are shown. The Fourier spectra of the oscillating part of the signals are presented in part b) of the figure. In Fig. 41 c) the instantaneous frequency, which was calculated as the inverse of the period of the oscillation, is shown as a function of the time delay.

As the pump density increases, the frequency of the phonon mode decreases and the peak becomes asymmetrically broadened. The shift in the instantaneous frequency is the largest at the earliest times. As the delay time increase the frequency

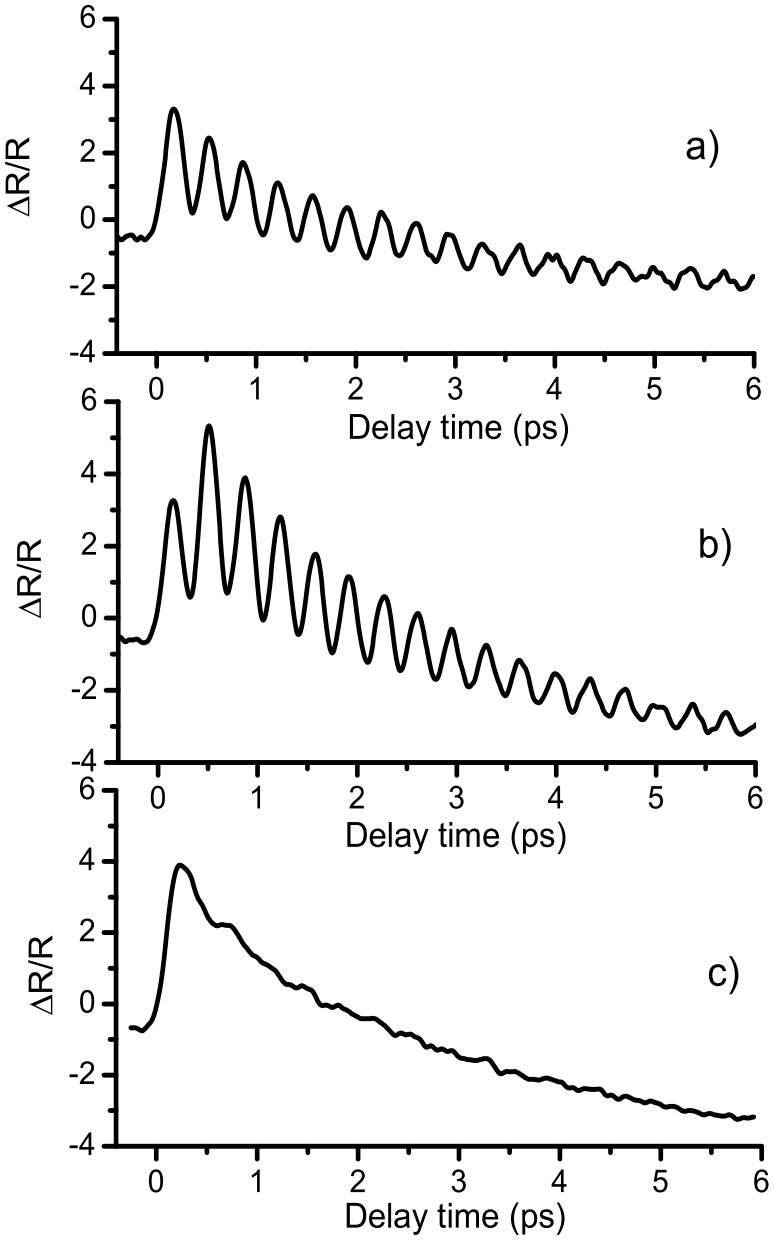

Fig. 40. Optical control of coherent optical phonons in a Bi film with two pump pulses. a) Excitation with one pump pulse, b) excitation with two pump pulses with a relative delay equal to the period of the oscillation, c) excitation with two pump pulses with a relative delay equal to the half a period of the oscillation.

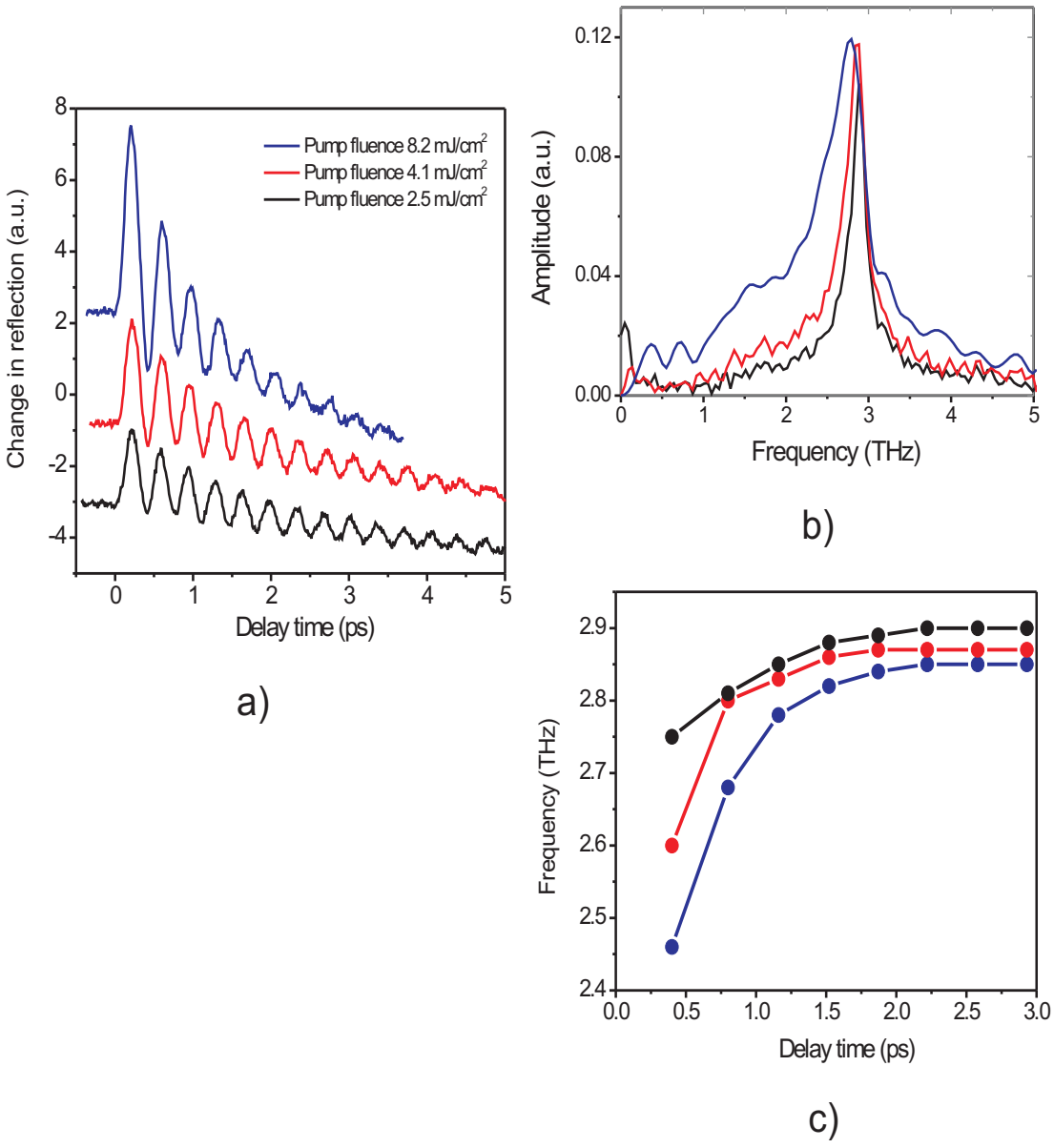

Fig. 41. Experimental results for excitation with a single pump pulse at different pump fluences: a) the transient reflectivity traces, b) the Fourier transform of the oscillating part of the signal, c) the instantaneous frequency as a function of the delay time.

relaxes toward its normal value (2.92 THz), although on the observed delay time scale it does not reach it.

The frequency shift observed in the experiment is "instantaneous", it is already present during the first oscillation. The energy transfer from the excited carriers to the lattice happens on a picosecond time scale, which means that any change in the lattice dynamics due to the increase in the lattice temperature will gradually increase on the same time scale. On contrast, the relaxation of the frequency at the later delay time toward its normal value is observed. So the effect of the lattice heating on the phonon mode frequency can be excluded.

A possible explanation of the decrease of the phonon mode frequency at the high photoexcitation can be attributed to the lattice softening due to excitation of the electrons from the valence band to the conduction band. The photoexcited carrier density at the maximum pump fluence used in this experiment is about 3×10^{21} cm^{-3} which corresponds to $\sim$2% of all the electrons in the valence band. The promotion of the electrons from the bonding to the anti-bonding state will result in weakening of the lattice and correspondingly will lower the frequency of the phonon mode. This softening of the lattice will be maximal at the initial moment of time, and the lattice will gradually go back to normal as the photoexcited carirers diffuse from the excited region.

Another possible explanation could be the effect of anharmonicity of the lattice. In this case the frequency of the lattice vibrations becomes a function of the amplitude of the atomic displacements in the lattice. The largest change in the frequency will also be at the initial moment of time, when the lattice displacement is maximal. As the amplitude of the lattice vibrations decreases, the phonon frequency will go back to the normal value.

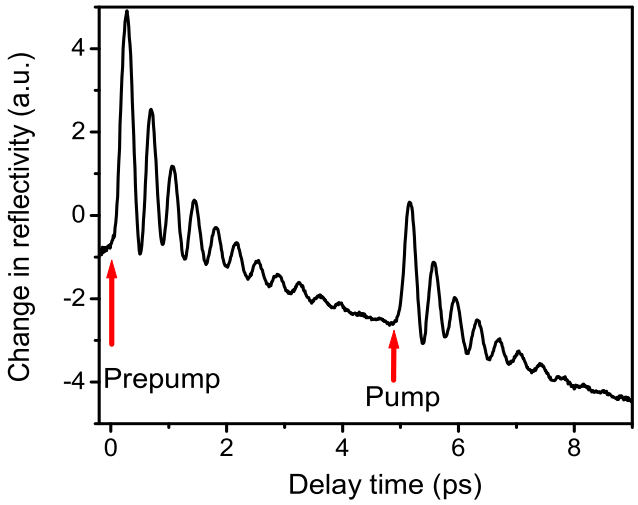

Fig. 42. Transient reflectivity signal obtained with two pump pulse excitation.

2. Excitation with two pump pulses

To separate the effect of the photoexcited carrier density from the possible effect of anharmonicity of the lattice, two pump pulses was used. This approach was applied by S. Hunsche *et. al* [62] in their studies of the dynamics of the optical phonons in Te. The first pulse (prepump) prepares the media by creating a density of the photo-excited carriers and the second pulse (pump) excites the coherent lattice vibrations.

In this experiment the fluence of the second pump was fixed at 1mJ/cm^2, while the fluence of the first pre-pump varied from 2 to 10 mJ/cm^2. The delay between the two pulses was set to 5 ps in order to reduce the interference between the coherent lattice vibrations excited by the pre-pump and the pump pulses. A typical signal is presented in Fig. 42. The experimental results for different prepump fluences is presented in Fig. 43. In part a) the time domain response induced by the pump pulse for different excitation levels of the pre-pump pulse is presented. In part b) the Fourier spectra of the time domain signals are shown.

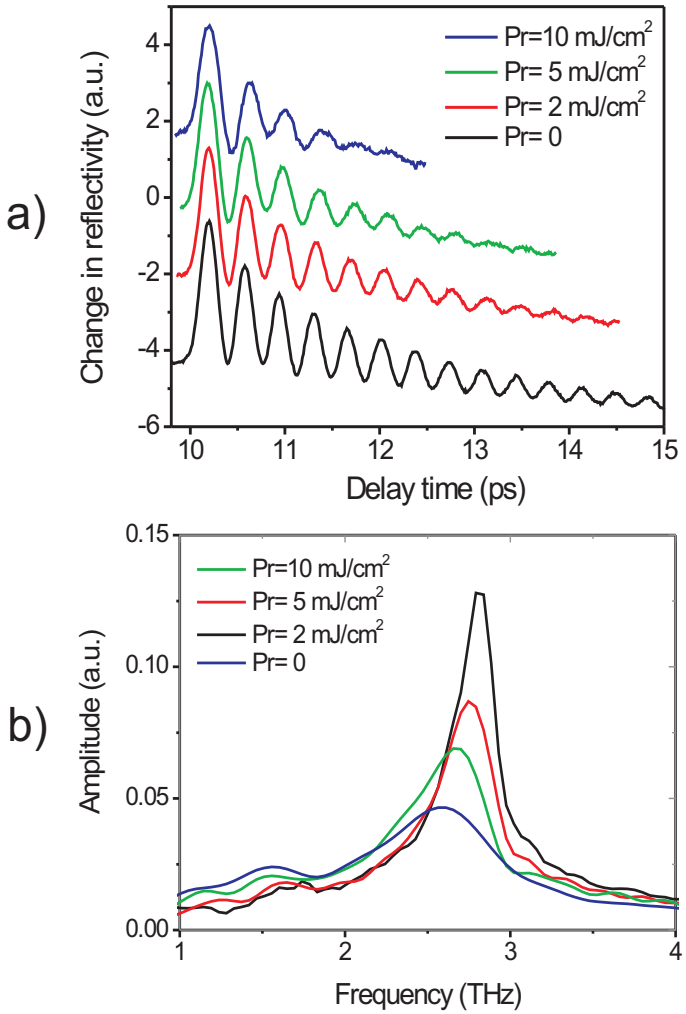

Fig. 43. Experimental results for excitation with two pump pulse experiments at different pump fluences: a) the transient reflectivity traces, b) the Fourier transform of the oscillating part of the signal.

The experimental data show that as the intensity of the prepump pulse increase the spectrum peak red-shifts and become broader. Since the energy of the pump pulse was kept constant in these measurements, we can conclude that the effect of the anharmonicity of the lattice can be excluded. This result is in agreement with the previous studies of photoexcited Bi by Murray *et al.* [50] where similar approach of excitation with two pump pulses was used.

3. Effect of the inhomogeneity of the excited carrier

The experimental data at the high excitation fluences show that the oscillation part of the signal decays faster at high excitation density. This effect can be explained by the inhomogeneity of the excited carriers.

In Bi, the absorption length for the pump pulse is about 17 nm, and the density of the photoexcited carriers is highly inhomogeneous. The results of the two pump probe experiment suggest that the frequency shift, observed at the high pump fluences, is a manifestation of the electronic lattice softening. That means that the frequency of the phonon mode depends on the density of the photoexcited carriers. In the experiment, the probe pulse is affected by the coherent lattice displacements within some depth inside the sample. The carrier density dependence of the phonon mode frequency will result in the inhomogeneous broadening of the response. To confirm the importance of this effect numerical simulations were carried out.

Following [62], the frequency dependence can be modeled as

$$f(N_{exc}) = f_0\sqrt{1 - \frac{N_{exc}}{N_c}}, \tag{4.31}$$

where N_c describes the critical excitation density, that leads to electronic melting of the lattice, and N_{exc} is the density of the excited carriers.

The results of the numerical simulations of the transient reflectivity are presented

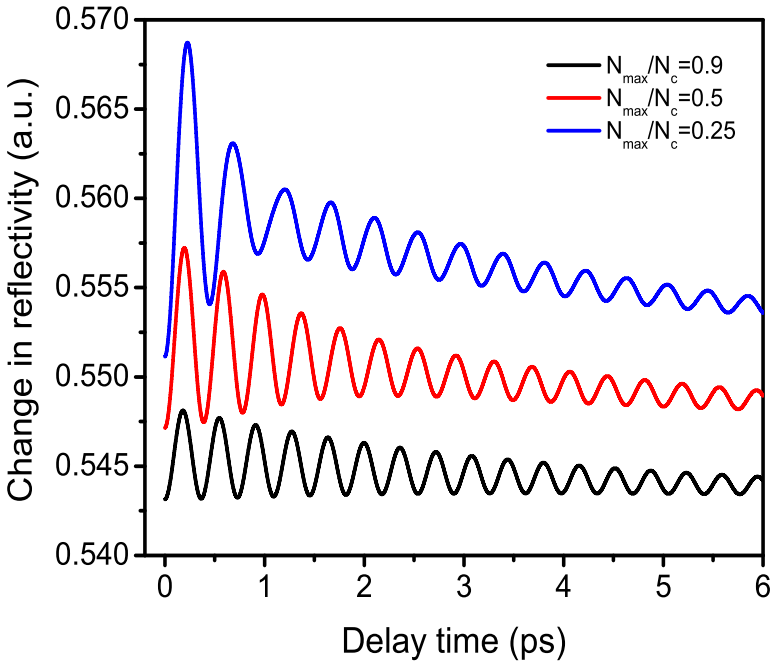

Fig. 44. The results of the numerical simulation of the transient reflectivity.

in Fig. 44. The traces are offset vertically for better visibility. N_{max} is the carrier density created by the pump pulse at the surface of the sample. The material parameters used in the calculations are n_r(400nm)=1.1, n_i(400nm)=2.4, n_r(800nm)=2.5, n_i(800nm)=5.0, f_0=2.93 THz, and the diffusion coefficient D=1.25 cm^2/s. For the homogeneous damping time the result from the low excitation measurements was used. The calculations show that the lifetime of the oscillations in the transint reflectivity signal decrease with increase in the photoexcitation carrier density. This additional damping is the result of inhomogeneous broadening caused by the variation of the excited carriers inside the sample.

CHAPTER V

CONCLUSIONS

The femtosecond two-color pump-probe technique was employed for measurements of high-frequency coherent oscillations in nanostructures and thin films. This technique proved to be a powerful tool for time-resolved measurements of these systems. The coherent acoustic vibrations of the fundamental breathing mode were observed in the Ag spherical particles with typical sizes 20-50 nm and Ag and Bi nanowires (about 70 nm and 200 nm diameters). The size dispersion of the nanowires was less than 10% which is less than the 50% found for the nanoparticles. The time resolution in the experiments of about 100 fs was determined by the duration of the femtosecond pulses used, and the typical frequencies of acoustic oscillations were in the range of 50-150 GHz. The experimental results show that the elastic properties of the spherical particle can be described by the homogeneous elastic model using elastic constants of the bulk material, neglecting also the aqueous environment of the solution.

Unlike previous measurements of nanoparticles, where transmission geometry was used, the transient responses of the samples with nanowires were measured using scattering configuration. When the intensity of the pump pulses was not very high, the oscillations had a simple sinusoidal form with attenuation. It was shown that the values of the acoustic longitudinal velocities of the samples of nanowires, obtained with the simple model of the isotropic elastic rod of a high aspect ratio, lie within the range of the elastic constants of the bulk material.

The transient acoustic response of Ag nanowires under excitation by intense laser radiation was studied. It was found that at the pump fluence above some value the shape of the experimental signal changes. This effect can be attributed to the laser induced softening or even melting of the material.

The transitional dynamics of coherent optical phonons in Bi at high excitation fluences was studied. The observed cosine-shape signals corroborate well with the displacive mechanism of the excitation. In the experiment the frequency of the optical phonons shifted from the value of about 2.92 THz at low pump intensities to about 2.45 THz near the damage threshold, above which a degradation of sample and the reduction of the signal was noticed. In the temporal evolution of the observed signal, the frequency of the oscillations gradually increased after the initial excitation interval, indicating that the density of the excited electrons decreased in time due to diffusion and relaxation. To asses the influence of the lattice anharmonicity compared to the effect of lattice softening the experiments with a pre-pump, where the excited state was mostly determined by the fluence of the pre-pump pulse, were carried out. In this case the strong variation of the optical phonon frequency was also observed, although the relatively low fluence of the pump pulse, used for monitoring the amplitude of optical phonons for different delay times was fixed. It is evident that the observed frequency shift is mostly due to the level of the electronic excitation and not due to the lattice anharmonicity, in agreement with the previous studies of the photoexcited Bi. Also we observed the increase of the optical phonon attenuation at higher fluences of the pre-pump, i.e. at higher electronic excitations. We performed modeling of the signals observed in the pump-probe experiments at high excitation levels taking into account the excitation inhomogeneity. By comparing with the experimental results we also came to the conclusion that the major contribution to the decay of the observed oscillations is due to the strong inhomogeneity in the excitation region and that the observed red-shift of the phonon frequency and its dynamics can be attributed to the lattice softening due to the electronic excitations.

REFERENCES

[1] A. Kolomenskii *et al.*, Phys. Rev. Lett. **79**, 1325 (1997).

[2] A. Lomonosov *et al.*, J. Acoust. Soc. Am. **105**, 2093 (1999).

[3] A. Kolomenskii and H. Schuessler, Phys. Rev. B **63**, 085413 (2001).

[4] R. Jin *et al.*, Nature **245**, 487 (2003).

[5] Y. Sun and Y. Xia, Science **298**, 2176 (2002).

[6] C. R. Martin, Science **266**, 1961 (1994).

[7] A. P. Alivisatos, Science **271**, 933 (1996).

[8] S. Tarucha *et al.*, Phys. Rev. Lett. **77**, 3613 (1996).

[9] K. Ma, Physics Today **46**, 24 (1993).

[10] M. Perner *et al.*, Phys. Rev. Lett. **85**, 792 (2000).

[11] N. D. Fatti *et al.*, J. Chem. Phys. **110**, 11484 (1999).

[12] J. Hodak, A. Henglein, and G. Hartland, J. Chem. Phys. **111**, 8613 (1999).

[13] M. Nisoli *et al.*, Phys. Rev. B **55**, 13424 (1997).

[14] H. Lamb, Proc. London Math. Soc. **13**, 189 (1882).

[15] T. Takagahara, J. Lumin. **15**, 129 (1996).

[16] N. Nishiguchi and T. Sakuma, Sol. State Commun. **38**, 1073 (1981).

[17] G. Garrett, T. Albrecht, J. Whitaker, and R. Merlin, Phys. Rev. Lett. **77**, 3661 (1996).

[18] J.-C. Diels and W. Rudolph, *Ultrashort Laser Pulse Phenomena* (Academic Press, San Diego, 1996).

[19] F. Gan, *Laser Materials* (World Scientific, Singapour, 1994).

[20] D. Strickland and G. Mourou, Opt. Commun. **56**, 219 (1985).

[21] A. Krishnan *et al.*, Phys. Rev. B **58**, 14013 (1998).

[22] E. Wong, P. Sheehan, and C. Lieber, Science **277**, 1971 (1997).

[23] M. Hu *et al.*, J. Am. Chem. Soc. **125**, 14925 (2003).

[24] G. Riveros *et al.*, Nanotechnology **17**, 561 (2006).

[25] G. Hartland and M. Hu, J. Phys. Chem. B **107**, 7472 (2003).

[26] G. Papavassiliou, Prog. Solid. St. Chem. **12**, 185 (1979).

[27] K. Kelly, E. Coronado, L. Zhao, and G. Schatz, J. Phys. Chem. B **107**, 668 (2003).

[28] R. Rosei, F. Antonangeli, and U. Grassano, Surf. Sci. **37**, 689 (1973).

[29] G. Mie, Ann. Phys. **25**, 329 (1908).

[30] U. Kreibig and M. Vollmer, *Optical Properties of Metal Clusters* (Springer, Berlin, 1995).

[31] R. Gans, Annln. Phys. **47**, 270 (1915).

[32] S. Link and M. A. El-Sayed, Int. Rev. in Phys. Chem. **19**, 409 (2000).

[33] A.Tamura, K. Higeta, and T. Ichinokawa, J. Phys. C **15**, 4975 (1982).

[34] C. Voisin, N. D. Fatti, D. Christofilos, and F. Vallee, Applied Surface Science **164**, 131 (2000).

[35] V. Dubrovskiy and V. Morochnik, Earth Phys. **17**, 494 (1981).

[36] B. Enustun and J. Turkevich, J. Am. Chem. Soc. **85**, 3317 (1963).

[37] J. Hodak, I. Martini, and G. Hartland, J. Phys. Chem. B **102**, 6958 (1998).

[38] G. Woehrle, J. Hutchison, S. Ozkar, and R. Finke, Turk. J. Chem. **30**, 1 (2006).

[39] C. V. D. Christofilos *et al.*, Phys. Rev. B **69**, 195416 (2004).

[40] J. Hodak, I. Martini, and G. Hartland, J. Chem. Phys. **108**, 9210 (1998).

[41] G. Hartland, J. Chem. Phys. **116**, 8048 (2002).

[42] H. Schwanbeck and U. Schmidt, Electrochimica Acta **45**, 4389 (2000).

[43] Y. Eckstein, A. Lawson, and D. Reneker, J. Appl. Phys. **31**, 1534 (1960).

[44] R. Bacon and C. Smith, Acta Met. **4**, 337 (1956).

[45] J. Neighbours and G. Alers, Phys. Rev. **111**, 707 (1958).

[46] T. Iida and R. Guthrie, *The Physical Properties of Liquid Metal* (Oxford University Press, New York, 1988).

[47] M. Hase *et al.*, Appl. Phys. Lett. **69**, 2474 (1996).

[48] J. Lannin, J. Calleja, and M. Cardona, Phys. Rev. B **12**, 585 (1975).

[49] M. Hase, M. Kitajima, S. Nakashima, and K. Mizoguchi, Phys. Rev. Lett. **88**, 067401 (2002).

[50] E. Murray *et al.*, Phys. Rev. B **72**, 060301 (2005).

[51] A. Kuznetsov and C. Stanton, *Ultrafast Phenomena in Semiconductors* (Springer-Verlag, New York, 2001), pp. 353–403.

[52] A. Kuznetsov and C. Stanton, Phys. Rev. Lett. **73**, 3243 (1994).

[53] H. Zeiger *et al.*, Phys. Rev. B **45**, 768 (1992).

[54] R. Merlin, Solid State Commun. **102**, 207 (1997).

[55] T. Stevens, J. Kuhl, and R. Merlin, Phys. Rev. B **65**, 144304 (2002).

[56] D. Bethune, J. Opt. Soc. Am. B **6**, 910 (1989).

[57] J. de Sandre, T. Missana, and C. Afonso, J. Appl. Phys. **80**, 7023 (1996).

[58] R. Atkinson and P. Lissberg, Thin Solid Films **17**, 207 (1973).

[59] R. Aagard, J. Opt. Soc. Am **64**, 1456 (1974).

[60] P. Wang and A. Jain, Phys. Rev. B **2**, 2978 (1970).

[61] A. Lenham, D. Treherne, and R. Metcalfe, J. Opt. Soc. Am. **55**, 1072 (1965).

[62] S. Hunsche and H. Kurz, Appl. Phys. A **65**, 221 (1997).

APPENDIX A

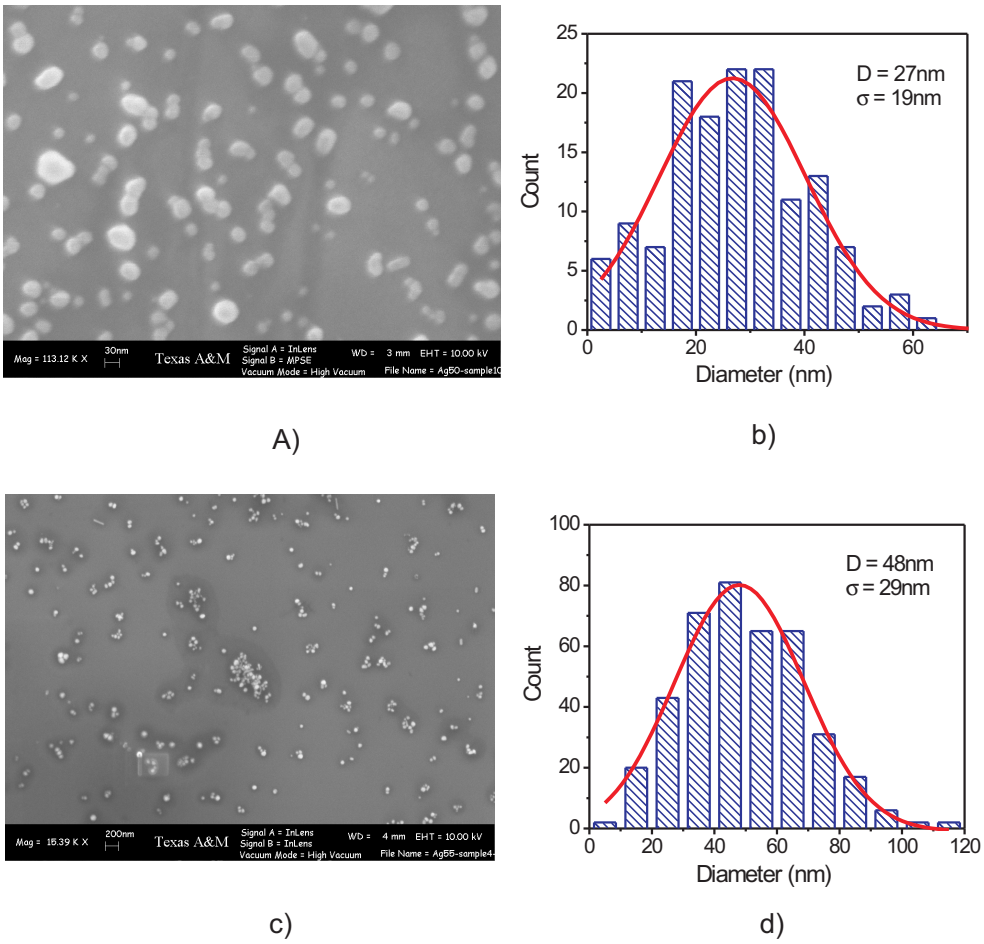

Fig. 45. SEM image and the size distribution of the small particles of the mean diameter d=27nm a), b) and the large particles of the mean diameter d=48 nm c), d).

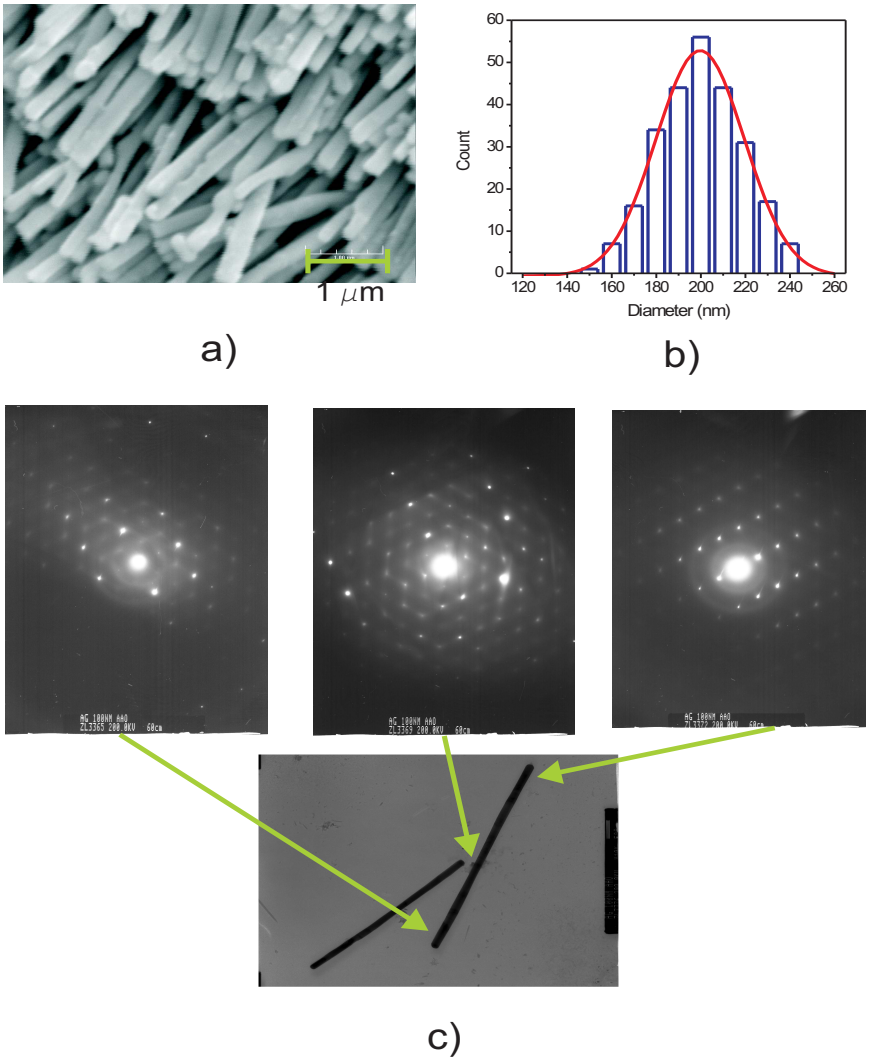

Fig. 46. An example of an SEM image of the large diameter silver nanowires a) and the size distribution b), and the SAED images measured at three points of a selected nanowire c).

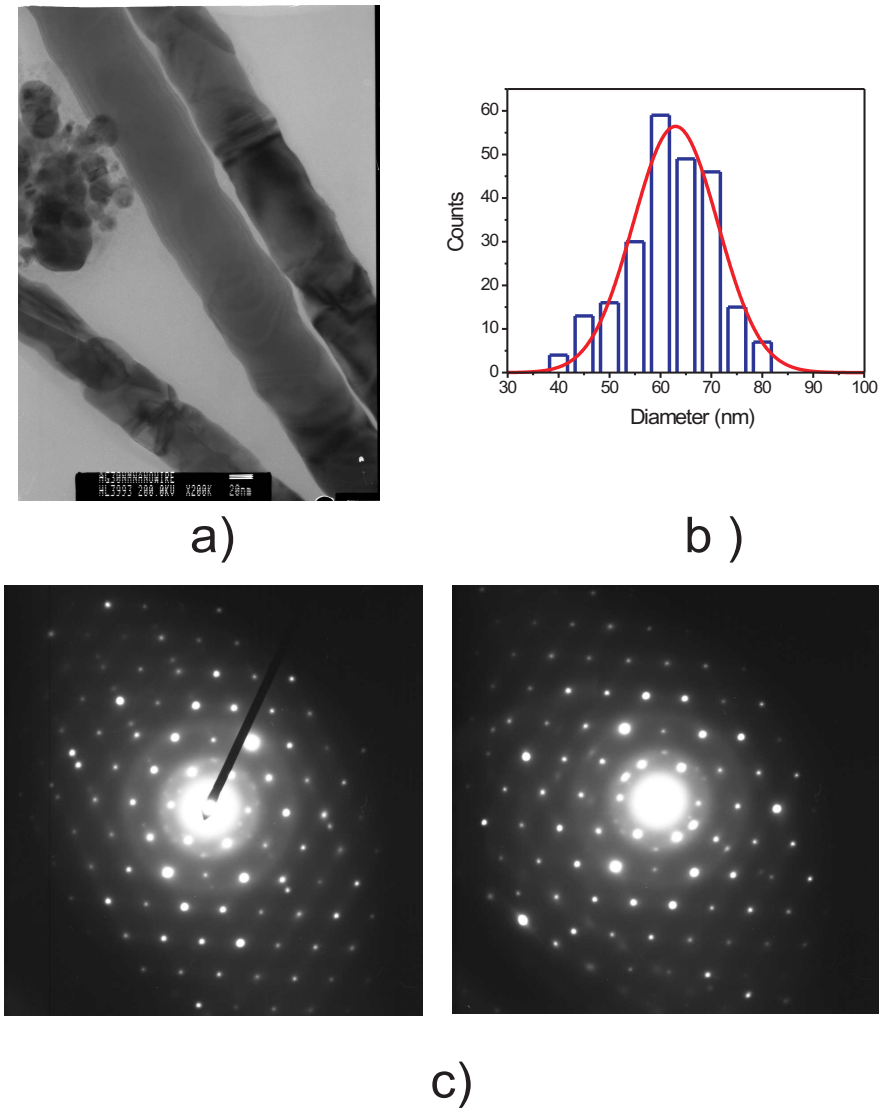

Fig. 47. An example of a TEM micrograph of small diameter Ag nanowires a), the size distribution of the that sample acquired from six images b), and the SAED images measured at two points of a selected nanowire c).

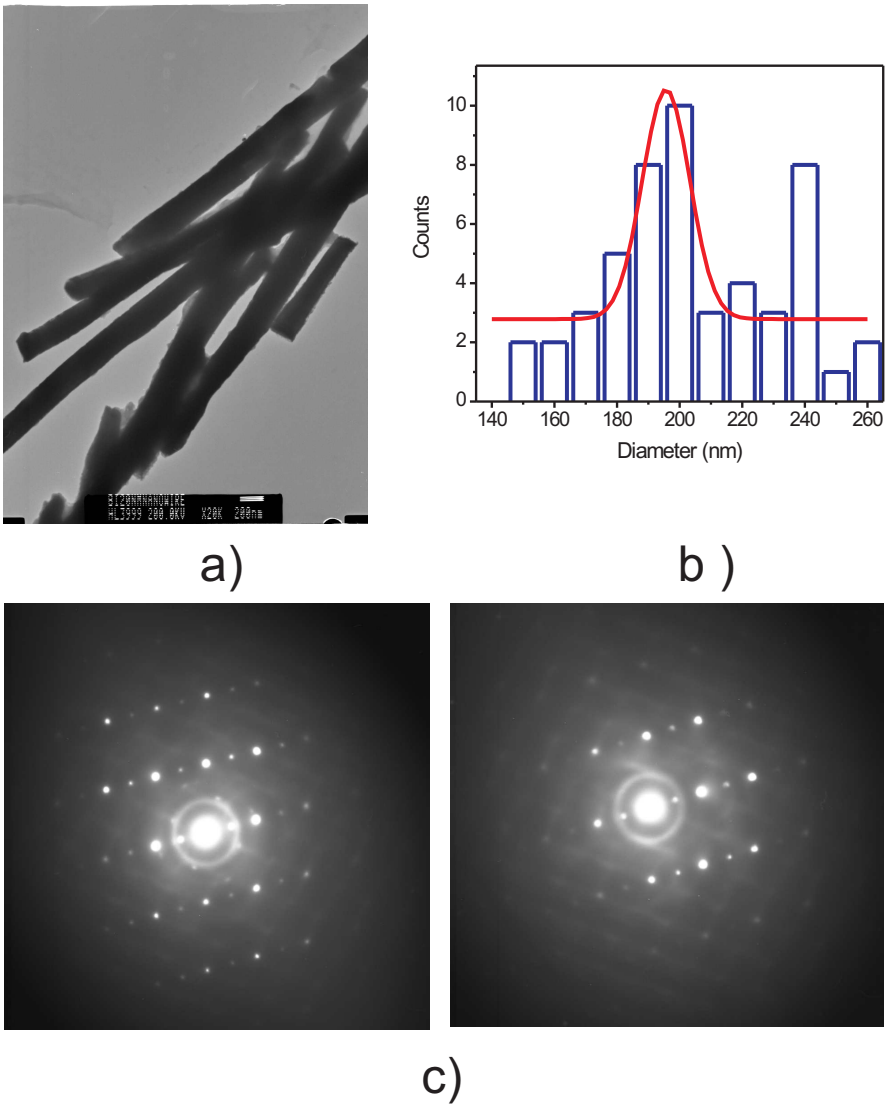

Fig. 48. A TEM micrograph of the large diameter Bi nanowires a), the size distribution of the that sample b), and the SAED images measured at two points of a selected nanowire c).

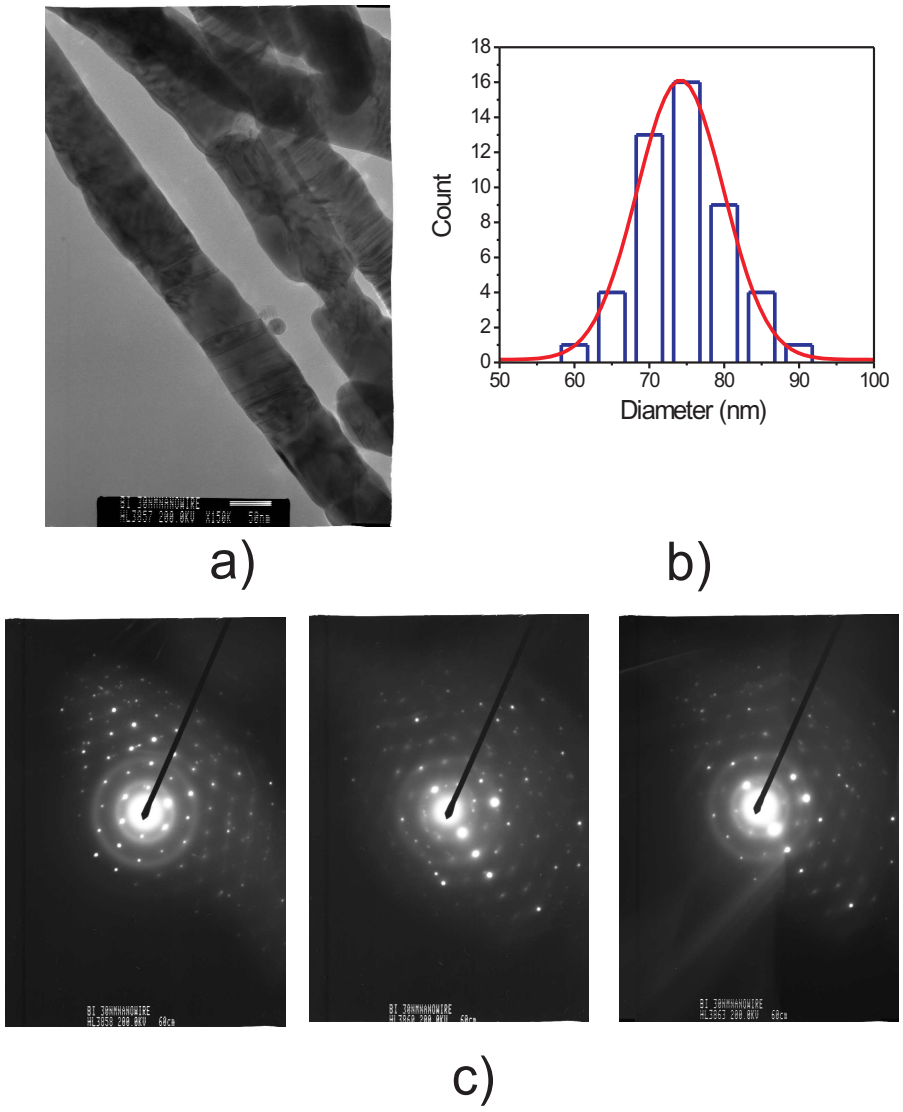

Fig. 49. A TEM micrograph of the small diameter Bi nanowires a), the size distribution for the that sample b), and the SAED images measured at three points of a selected nanowire c).

APPENDIX B

DETERMINATION OF LINEAR AND NONLINEAR ELASTIC PARAMETERS FROM LASER EXPERIMENTS WITH SURFACE ACOUSTIC WAVE PULSES.

doi:10.1016/S0584-8547Z03.00069-7

APPENDIX C

FOCAL TRANSFORMATION AND THE GOUY PHASE SHIFT OF CONVERGING ONE-CYCLE SURFACE ACOUSTIC WAVES EXCITED BY FEMTOSECOND LASER PULSES.

APPENDIX D

NONLINEAR SURFACE ACOUSTIC WAVE PULSES IN SOLIDS: LASER EXCITATION, PROPAGATION, INTERACTIONS.

VITA

Serguei Jerebtsov was born in Leninsk-Kuznetskiy, Russia. He received a B.S. degree from Moscow Engineering and Physics Institute, Moscow, Russia. He entered a Ph.D. program at the Department of Physics Texas A&M University in 1999 and graduated in May 2007. His current address is Department of Physics, Texas A&M University, College Station, TX 77843-4242.

The typist for this thesis was Serguei Jerebtsov.